Impact of changing concavity indices on channel steepness and divide migration metrics

Boris Gailleton[1], Simon M. Mudd[1], Fiona J. Clubb[2], Stuart W.D. Grieve[3], and Martin D. Hurst[4]

[1]School of GeoSciences, University of Edinburgh, UK [2]Department of Geography, Durham University, UK [3]School of Geography, Queen Mary University of London, UK [4]School of Geographical & Earth Sciences, University of Glasgow, UK

Key Points:

- We develop metrics to understand the variability of the concavity index in a given landscape, to help guide authors on how reliable a single value of θ will be if applied across a landscape.
- We compute the values of concavity index (θ) in basins across the globe (N=5033). The central tendency is 0.425, corroborating previous studies, but there is a large range in values, with interquartile range of 0.225–0.575.
- We find that the channel steepness index (k_{sn}), the χ coordinate and knickpoint extraction are all sensitive to the value of θ, with implications for river profile analysis and the detection of migrating drainage divides in landscapes with variable concavities.

Corresponding author: Boris Gailleton, School of GeoSciences, University of Edinburgh, Drummond Street, Edinburgh, EH8 9XP, UK, s1675537@sms.ed.ac.uk

Abstract

The concavity index, θ, describes how quickly river channel gradient declines downstream. It is used in calculations of normalized channel steepness index, k_{sn}, a metric for comparing the relative steepness of channels with different drainage area. It is also used in calculating a transformed longitudinal coordinate, χ, which has been employed to search for migrating drainage divides. Here we quantify the variability in θ across multiple landscapes distributed across the globe. We describe the degree to which both the spatial distribution and magnitude of k_{sn} and χ can be distorted if θ is assumed, not constrained. Differences between constrained and assumed θ of 0.1 or less are unlikely to affect the spatial distribution and relative magnitude of k_{sn} values, but larger differences can change the spatial distribution of k_{sn} and in extreme cases invert differences in relative steepness: relatively steep areas can appear relatively gentle areas as quantified by k_{sn}. These inversions are function of the range of drainage area in the considered watersheds. We also demonstrate that the χ coordinate, and therefore the detection of migrating drainage divides, is sensitive to varying values of θ. The median of most likely θ across a wide range of mountainous and upland environments is 0.425, with first and third quartile values of 0.225 and 0.575. This wide range of variability suggests workers should not assume any value for θ, but should instead calculate a representative θ for the landscape of interest, and exclude basins for which this value is a poor fit.

Plain Language Summary

The elevation profiles of rivers are commonly used to interpret their tectonic and erosion history. The slope of river channels tends to decline downstream, and this decline can be described by a river's concavity. Estimating the concavity is important when comparing river profiles across a region, and using an assumed value for concavity may result in spurious interpretations.

1 Introduction

For over a century, geoscientists have recognised the potential of fluvial geomorphology to unravel links between landscape evolution and external forcing (e.g. Gilbert, 1880; Davis, 1899). In his review of physical geography at the time, de Lapparent (1896) outlined a number of basic observations underpinning modern geomorphology: the systematic concave up shape of river long profiles, the hypothesis that erosion is correlated with channel gradient, and that lithologic contrasts and inherited tectonic structures influence river profile form. The geometry of river profiles later became one of the key tools for geoscientists in the first half of the 20$^{\text{th}}$ century for interpreting landscapes (e.g. Knopf, 1924).

Assuming that channel gradient encodes information about erosion rates, lithology, or other factors, you are faced with a fundamental problem: the concave nature of a typical river obscures relative steepness, as channel gradient has the pernicious tendency to increase towards the headwaters of a catchment. That is, how can one tell if a headwater channel is steeper, in a way that is meaningful for interpreting landscape evolution, than a section of the river some distance downstream? Some normalization is therefore required to compare river sections with different drainage areas. Morisawa (1962) noted a power law relationship between gradient and drainage area, which led to a means of normalizing river gradients. Flint (1974) formalized these observations into the slope–area relationship with a concavity index (θ), which describes how quickly river gradient decreases with increasing drainage area, and a steepness index (k_s) that describes the relative steepness of a reach regardless of its drainage area:

$$S = k_s A^{-\theta} \tag{1}$$

where S is the gradient of elevation along the channel ($S = dz/dx$ where z is the elevation and x the flow distance); and A is the drainage area. This relative steepness index k_s, in particular, has been widely used in geomorphology because of its empirically observed positive correlation with erosion rates (e.g., Safran et al., 2005; DiBiase et al., 2010; Cyr et al., 2010; Scherler et al., 2014; Ouimet et al., 2009; Kirby & Whipple, 2012; Mandal et al., 2015; Harel et al., 2016), supported by a theoretical underpinning (Whipple & Tucker, 1999). The value of steepness index derived from drainage area and gradient depends on the value of the concavity index, so in order to compare different channels, the steepness index is typically calculated with a single value of θ, resulting in a "normalized" steepness index (k_{sn}) (Wobus et al., 2006). Despite the importance of constraining θ for calculating channel steepness, it is often assumed in many studies that $0.4 < \theta < 0.6$ (e.g. Tucker & Whipple, 2002; Whipple, 2004; Kirby & Whipple, 2012).

Numerous authors have attempted to extract concavity indices from topographic data. For example, Tucker and Whipple (2002) compiled concavity indices using slope–area regression from ten previous studies, aggregating 27 different sites, and found concavity indices ranging from 0.11–1.13. Whipple (2004) argued that if you limit extraction of the concavity index to bedrock rivers with homogeneous substrates, homogeneous uplift fields and time invariant uplift, concavity indices converge to a range between 0.4–0.7.

Whipple (2004) went on to articulate circumstances in which concavity indices may fall outside this range. They argued that low concavity indices ($\theta < 0.4$) can result from drainage basins influenced by debris flows (e.g. Stock & Dietrich, 2003) or from downstream increases in incision rate or rock strength (Kirby & Whipple, 2001). Alluvial rivers can also have low concavity values: Gasparini et al. (2004) used a numerical model to predict that finer sediment could result in low concavity values (< 0.4) when either grain size was less than 100 mm in homogeneous sediment or if there was a high percentage of sand in mixed gravel and sand rivers. Whipple (2004) suggested that high concavities ($\theta > 0.7$) could result from downstream transitions to full alluvial conditions with bedrock reaches in headwaters, and also noted the findings of Kirby and Whipple (2001) that high concavity can result from downstream increases in rock strength or incision rate. Extreme concavity values ($\theta > 1.0$) can also result from large knickpoints (e.g. Schoenbohm et al., 2004). Furthermore, Zaprowski et al. (2005) found that channel concavities varied systematically across a gradient in mean annual precipitation and precipitation intensity, with higher concavities associated with a more intense hydrological settings on the high plains of the western USA.

In this contribution, we aim to question the common assumption that a narrow range of θ values is appropriate for the majority of Earth's landscapes. To do this, we attempt to constrain the range of concavity indices present both within and between a wide range of different study sites. We compare different methods of estimating the most likely values of θ and refine existing methods of quantifying the uncertainty in choosing a most likely value of θ. We then examine the impact of using a poorly-constrained concavity value on estimates of k_{sn} and the metric χ, which integrates drainage area along channels and has been used to detect drainage divide migration (Willett et al., 2014), and highlight the potential risks of misinterpretation in such cases.

2 Determining the concavity index

2.1 Concavity index derived from slope–area data

A common approach to deriving fluvial profile concavity is to transform equation 1 into logarithmic space:

$$log[S] = log[k_s] * -\theta\, log[A] \tag{2}$$

where θ is the gradient of log[A]–log[S] plots and k_s the intercept where log[A] = 0 (i.e., where $A = 1$ m^2 if areas are reported in square meters). Assuming k_s is a constant, θ can be determined by linear regression of log[A]–log[S]. This logarithmic slope–area method has been widely used to determine both concavity and channel steepness (e.g. Wobus et al., 2006; Kirby & Whipple, 2012; Whipple et al., 2013).

However, the use of raw S–A data has limitations: the seminal Wobus et al. (2006) paper includes the word "pitfalls" in the title. DEM data is inherently noisy (e.g. Wobus et al., 2006; Perron & Royden, 2013), either because of natural noise in river profiles or due to errors in the acquisition methods (e.g. airborne lidar or satellite altimetry), and taking the gradient of noisy data amplifies that noise (e.g. Perron & Royden, 2013). In addition, tributaries result in large jumps in drainage area, resulting in major gaps along the log[A] axis. Between tributaries, drainage area increases slowly, but channel gradient can vary dramatically due to heterogeneity in local river bed conditions. This means that some form of averaging or binning must be used on the raw slope–area data in order to extract k_s and θ values.

We illustrate difficulties in extracting the concavity and steepness indices from S–A in Figure 1. This figure contrasts a theoretical case (panel **a**) with real data that considers the basin as a whole (panel **b**), each different tributary channel individually (panel **c**), or solely the main stem channel (panel **d**). Values of θ can vary substantially in the same drainage basin depending on the S–A data used, as shown by the histograms of best-fit populations of θ within the inset plots in panels **b,c,d**. This does not suggest that S–A data is unsuitable for extracting landscape metrics: steepness indices derived from this method have been shown to correlate well with other landscape properties such as erosion rates and tectonic activity in a range of contexts (e.g. Kirby & Whipple, 2012). However it highlights the potential difficulties and uncertainties in using this technique to extract θ or k_s, particularly across large areas where θ might vary spatially.

2.2 Concavity index from the integral approach

These problems with the slope–area approach have led to the development of alternative methods in recent years. One such technique is to integrate drainage area along flow distance, which was first suggested by Royden et al. (2000) and further developed in Perron and Royden (2013) as a way to circumvent uncertainties associated with calculating gradient from noisy topographic data. Following Whipple et al. (2017) we can integrate equation 1, resulting in

$$z(x) = z(x_b) + \left(\frac{k_s}{{A_0}^\theta}\right) \int_{x_b}^{x} \left(\frac{A_0}{A(x)}\right)^\theta dx, \tag{3}$$

where $z(x_b)$ is the elevation of the channel at some base level, and A_0 is a reference drainage area, introduced to nondimensionalize the area term within the integral in equation (3). We can then define a longitudinal coordinate, χ:

$$\chi = \int_{x_b}^{x} \left(\frac{A_0}{A(x)}\right)^\theta dx. \tag{4}$$

The coordinate χ has dimensions of length, and is defined such that at any point in the channel:

$$z(x) = z(x_b) + \left(\frac{k_s}{{A_0}^\theta}\right)\chi. \tag{5}$$

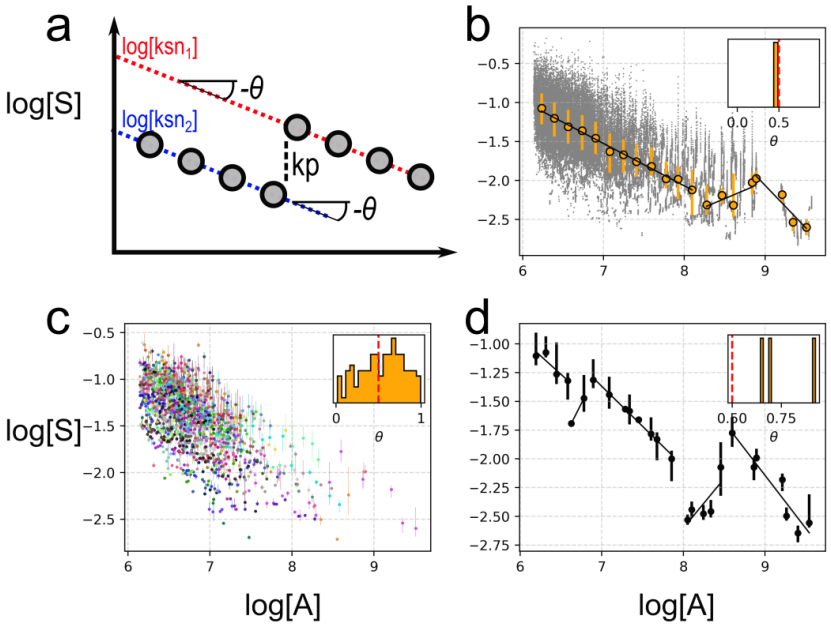

Figure 1. Example slope–area plots. **a.** An idealized channel with slope and area following equation 1. θ is uniform and a clear knickpoint separates two populations of k_{sn}. **b.** Slope–area data from a real watershed (the Buzău river in Romania, 3000 km^2, outlet coordinates latitude 45.20 and longitude 26.75 in WGS84). Each grey point represents gradient calculated over a vertical window of 20 meters; data derived from the ALOS World 3D 30 dataset. Note the noise and irregularity of data spacing along the axes. In orange, data is binned by drainage area and concavity is calculated using a segmentation algorithm described in Mudd et al. (2014). Only one of the resulting segments has a concavity between 0 and 1: the inset in panels **b,c, and d** show histograms of concavity values between 0 and 1 based on segmentation of S–A data. Panel **c.** shows slope–area data binned by drainage area for all tributaries of the same watershed. The population of θ is obtained by using the segmentation of slope–area data in each each tributary. Panel **d.** shows data for the main stem channel only.

Equation 5 has two key predictions: firstly, assuming that k_s and θ are spatially constant, there will be a linear relationship between χ and elevation for a single channel; and secondly, that tributaries will be collinear with the main stem. If the linearity prediction is true, θ can be calculated for a river by iterating through a range of θ values for a given network and selecting the value with a best-fit linear relationship between χ and elevation (Perron & Royden, 2013). In many real landscapes which are undergoing transient adjustment, however, k_s may vary spatially. Alternative approaches have attempted to fit a number of linear segments to χ-elevation data to circumvent this problem (Mudd et al., 2014, 2018).

The collinearity prediction provides a second independent metric of calculating the concavity index (θ) that does not assume that river profiles are linear in χ-elevation space. Instead it assumes that a point anywhere on the channel network with the same χ value will have the same elevation. This has been used as the basis for a number of techniques which calculate the concavity index by minimising the scatter between points on tributaries with the main stem channel (Goren et al., 2014; Hergarten et al., 2016; Mudd et al., 2018). The collinearity test would be rather restrictive, however, if it were limited to landscapes where k_s were uniform. Royden and Perron (2013) used solutions of the stream power law to show that collinearity holds even if there are perturbations to the erosion rate that propagate upstream through the channel network. The stream power law has many assumptions (e.g. Lague, 2014), but we can alternatively use geometric relationships to show that collinearity is indicative of the most likely concavity index without invoking stream power.

Two centuries ago, Playfair (1802) observed that tributary junctions often featured channels joining at a common elevation: waterfalls are not systematically present at tributary junctions. This must mean that the two contributing streams need to have eroded at the same rate as the river just downstream of the junction. Niemann et al. (2001) expanded on this geometric observation and derived an expression for the migration rate of a local channel steepening or knickpoint (called its celerity, Ce_h [L/T]) of:

$$Ce_h = \frac{1}{S_2 - S_1}\Delta E, \tag{6}$$

where S_1 is the channel slope prior to disturbance, S_2 is the channel slope after disturbance (e.g., due to a change in incision rate E), and ΔE is the difference between the incision rate before and after disturbance (E_1 and E_2 in units of length per time, $\Delta E = E_2 - E_1$). Following Wobus et al. (2006) we can introduce drainage area into equation (6) by replacing the slope terms using equation (1).

$$Ce_h = \frac{E_2 - E_1}{k_{s2} - k_{s1}}A^{\theta}. \tag{7}$$

Once Ce_h is known, we can calculate the vertical celerity (Ce_v) which is simply the horizontal celerity multiplied by the local slope after disturbance S_2 (Wobus et al., 2006). The vertical celerity of a disturbance to the channel network is independent of drainage area:

$$Ce_v = \frac{E_2 - E_1}{k_{s2} - k_{s1}}k_{s2}. \tag{8}$$

Equation (8) implies that, under conditions of spatially homogeneous uplift and constant erodibility (i.e., channels with the same slope and drainage area erode at the same rate), then changes in slope will propagate vertically in elevation at a constant rate. If we begin with a landscape with constant k_s as described in equation 5 that has a collinear

channel network, and propagate changes in slope at a constant vertical celerity, the network will remain collinear even if k_s becomes spatially heterogeneous.

2.3 Can we know if a concavity index is "correct"?

The calculations of concavity index presented above are based on models of detachment-limited incision. A number of authors have also attempted to derive the concavity index from transport-limited models (e.g., Whipple & Tucker, 1999; Wickert & Schildgen, 2019). Although these models are a promising approach for understanding the fluvial concavity index, it is currently challenging to test these predictions by quantifying the correct concavity index from field observations.

An alternative approach is to create simulated topography using a model that bears some resemblance to measured incision processes, impose a concavity index upon this model, and then test if the topographic methods are able to correctly extract the imposed concavity index (e.g. Mudd et al., 2018). In spatially homogeneous, steady state landscapes, both methods could extract the correct concavity index, which is unsurprising since this situation just produces a topographic surface exactly obeying equation 1. If the modelled landscapes were perturbed by changing uplift rates, or variations in erodibility, then Mudd et al. (2018) found that the slope–area method could not reliably be used to identify the imposed concavity index. In contrast, Mudd et al. (2018) found the collinearity approach could identify the imposed concavity index under spatial and temporal heterogeneity that might be found in a natural landscape. Therefore, for the rest of this paper, we primarily focus on extracting the concavity index using the collinearity method.

3 Impact of varying concavity on the channel steepness index

The channel steepness index in equation 1 (k_s) depends on the concavity index, meaning that a reference value of θ (θ_{ref}) must be set to compare k_s values across multiple basins (Wobus et al., 2006). This results in "normalized" values of the steepness index, k_{sn}. Values of the normalized steepness index, k_{sn}, have been widely correlated with either uplift rates, inferred from a range of indicators such as dated terraces (e.g., Snyder, 2000), or erosion rates, usually inferred from the concentrations of in-situ cosmogenic nuclides such as ^{10}Be (e.g., Lal, 1991). In many such studies, there is a clear positive correlation between k_{sn} and inferred erosion and uplift rates (e.g., Kirby & Whipple, 2001; Safran et al., 2005; DiBiase et al., 2010; Cyr et al., 2010; Scherler et al., 2014; Ouimet et al., 2009; Mandal et al., 2015; Harel et al., 2016). Broadly speaking, these results indicate that steeper channels do reflect faster erosion rates, if one controls for other factors such as lithology.

If we believe that channel steepness can serve as a proxy for erosion rates, and that erosion rates are correlated with uplift rates, then it follows that channel steepness may be a powerful tool for detecting spatial variations in tectonic activity (e.g., Kirby & Whipple, 2012; Whittaker, 2012). However, k_{sn} is a function of the concavity index. If we choose the incorrect value of the concavity index, what is the potential for misinterpreting the spatial distribution of relative channel steepness, and therefore uplift patterns?

Figure 2 depicts scenarios where changing the value of the concavity index will result in substantially different interpretations of the spatial variation in channel steepness. Figure 2a illustrates a catchment with spatial heterogeneity in θ. If one θ is used for the entire catchment this can lead to dramatic differences in the calculated k_{sn} values. This behavior is also expected in χ space, as shown in Figure 2b, where the steep slope patches, which are interpreted as representing faster erosion, appear in different locations depending on the value of θ. Panels **c.** and **d.** also highlight how, depending

on the choice of θ, one might find two clearly separated values of k_{sn} within the channel network or a range of values (see inset in panel **c.**).

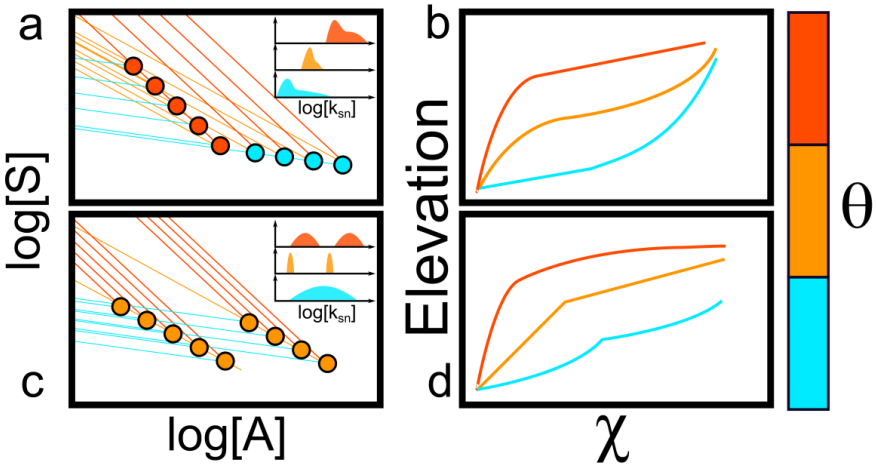

Figure 2. Schematic diagram exploring ways in which changing the values of the concavity index lead to differing interpretations of tectonics or erosion based on channel steepness index. Blue, orange and red colors represent low, medium and high concavities, respectively. The left column depicts S–A data for two idealized catchments and the right column shows the corresponding χ-elevation plots. The value of k_{sn} for each point in these basins will be determined by the point at which the lines intersect with the vertical axis at $\log[A] = 0$. Catchment 1 (top row) represents a catchment with spatial variation in concavity from a low-concavity outlet to high-concavity headwaters. Selecting one index for the entire catchment will alter the distribution of k_{sn} values as shown in the inset plots. Catchment 2 (bottom row) represents a catchment with one concavity but spatial variation in k_s. This spatial variation in k_s will only be detected if the correct concavity value is chosen.

Conceptual diagrams such as Figure 2 highlight the uncertainties in k_{sn} that are generated by uncertainties in θ. However, it is not straightforward to predict where these distortions will be greatest. One issue is that the relationship between k_{sn} and θ is non-linear: the order of magnitude of the steepness values for different values of θ are not directly comparable. In addition, the noise of S data and sparsity of A data, caused by jumps in A at junctions, require the use of data-loss methods such as binning (e.g. Wobus et al., 2006). This disconnects single points in a channel from S–A data and therefore hinders our ability to check binned values against field knowledge. Although the χ transformation offers a means to circumvent some of these issues (Perron & Royden, 2013), it is calculated with a fixed θ value, meaning that landscape–scale χ transformations may be distorted by the choice of θ (Figures 2b and d. Our study is focused on assessing the extent of this distortion and proposing metrics to estimate which θ value will least distort values of k_{sn}.

4 Methods

4.1 Quantifying concavity using disorder

We begin by looking at the uncertainty of θ values for a single basin. We use the disorder metric, first suggested by Goren et al. (2014), that is a measure of how far tributaries depart from the main stem river and amongst themselves in χ–elevation space (e.g. Goren et al., 2014; Hergarten et al., 2016; Mudd et al., 2018; Shelef et al., 2018). Our implementation follows the method of Hergarten et al. (2016). It ranks every point in the channel network by increasing elevation, and then checks to see if the associated χ coordinates are similarly ranked (or not):

$$R = \sum_{i=1}^{N} \left| \chi_{s,i+1} - \chi_{s,i} \right|, \tag{9}$$

where the the subscript s, i represents the i^{th} χ coordinate that has been sorted by its elevation. This sum, R, is minimal if elevation and χ are related monotonically. However it scales with the absolute values of χ, which are sensitive to the concavity index (see equation 4), so following Hergarten et al. (2016) we scale the disorder metric, D, by the maximum value of χ in the tributary network (χ_{max}):

$$D = \frac{1}{\chi_{max}} \left(\sum_{i=1}^{N} \left| \chi_{s,i+1} - \chi_{s,i} \right| - \chi_{max} \right). \tag{10}$$

The most likely concavity index is that which results in the lowest value of D for the river network: a perfectly collinear population of points would have $D = 0$ (Hergarten et al., 2016). To constrain uncertainty, Mudd et al. (2018) created subset networks formed from the trunk stream and every possible combination of three tributaries (Figure 3). The minimum D value was calculated for all of these combinations by iterating over θ values, creating a population of best fit concavity index values from all the combinations. The median and interquartile range were then reported.

Several authors have shown this method is effective in identifying the most likely concavity index for a watershed (Hergarten et al., 2016; Mudd et al., 2018). However, as explained in section 3, one may be compelled to use a different value of θ for a particular watershed, for example if one is comparing values of normalized channel steepness and needs to apply a constant θ value across the landscape to generate k_{sn} data. We would like to know how well this fixed value of θ performs for multiple basins. We have therefore adapted the disorder approach to quantify sensitivity to changing θ. For every combination of tributaries, we calculate a value of D for a range of θ values. We then normalise each value of D by the maximum disorder value (D_{max}) from that range:

$$D^* = \frac{D}{D_{max}} \tag{11}$$

This results in a population of D^* values for every value of θ, and these values vary between 0 and 1 (Figure 3). If the dataset is perfectly collinear, then D will equal 0 (Hergarten et al., 2016), so normalizing by D_{max} means D^* spans from the maximum disorder to perfectly collinear channel networks. We can then quantify the median and lower quartile of D^* as a function of θ, and from these derive estimates of the most likely θ value as well as some indication of how well constrained this value is. If the best fit concavity index is well constrained, the D^* values will have a sharply defined minimum, whereas a poorly defined value will have a very broad range of D^* values as illustrated in Figure 3c. We calculate D^* to provide metrics reflecting how well constrained θ is for a given watershed.

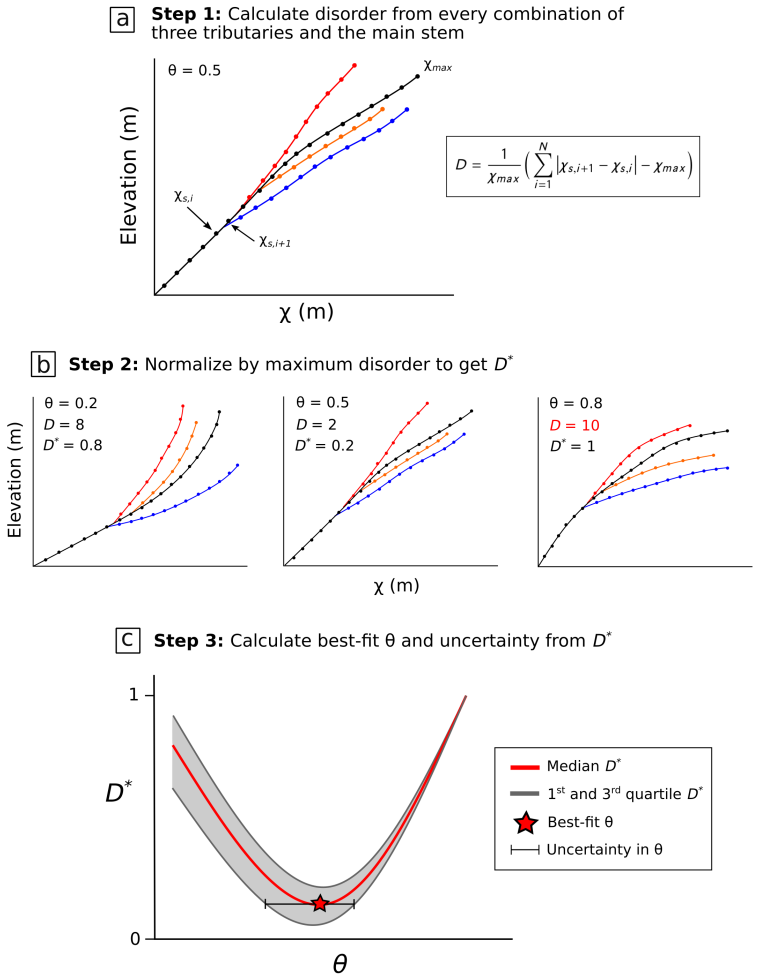

Figure 3. Method to determine best fit θ from all stream elevation data in a catchment by measuring the normalised disorder in χ values ranked by corresponding increasing elevation within the catchment (A). Uncertainty is constrained through a bootstrapping approach to measure the disorder for all possible combinations of three tributaries plus the main stem (B) to build an uncertainty range for D^* across the range of plausible θ values (C).

Finding the value that minimises the disorder might suggest the most likely value for a watershed. However it is also important to quantify the goodness of this value, *i.e.* if a range of values would result in similar disorder metrics, or alternatively if small changes to the value of θ would lead to much greater disorder. We therefore developed a further metric for quantifying the uncertainty of θ within a watershed. The most likely value of θ is defined by the minimum value of median D^* from all combinations of tributaries extracted for each value of θ (Figure 3c). Alongside the median we also calculate the first quartile: these values are lower than the median for each value of θ, so we draw a horizontal line from the minimum of the median D^* values and mark where this intersects with the first quartile D^* values at both lesser and greater values of θ (Figure 3, panel **C**). We then define the uncertainty range, R_θ, as the distance between these two points (max_{Q1} and min_{Q1}):

$$R_\theta = max_{Q1} - min_{Q1} \tag{12}$$

Lower values R_θ mean that there is less uncertainty on the best-fit θ (Figure 4). We can further assess the goodness of fit for θ for entire landscapes by calculating the cumulative distribution (CDF) of R_θ values across multiple basins. The shape of the cumulative distribution is a direct proxy of the cleanness of the best-fits: a steep CDF with low values would mean that the majority of basins had relatively low uncertainties on θ, whereas a more gradually increasing CDF would indicate that the landscape exhibits a wider range of uncertainty on θ.

The technique outlined above allows us to calculate the best-fit theta value for one particular basin. However, D^* is less useful if we wish to constrain the most likely value of θ across multiple watersheds, as different basins will have a different minimum value. Therefore, we also calculate a disorder metric normalized by the range of disorders within a basin, which we call D_r^*:

$$D_r^* = \frac{D - D_{min}}{D_{max} - D_{min}} \tag{13}$$

We can calculate D_r^* for the reference value of θ (θ_{ref}) across every basin in the landscape. If the best-fit θ for a particular basin is equal to θ_{ref}, then D_r^* for that basin will be 0. We can therefore interrogate the distribution of D_r^* values for the landscape to determine how well-constrained θ_{ref} is, and therefore how reliable our estimates of normalized channel steepness will be.

4.2 Quantifying spatial variations of θ using S–A

The disorder metric outlined in Section 4.1 relies on comparing the main stem channel with a number of tributaries. In some cases, either where basins have very few tributaries, or if concavity along a specific channel is of interest this method is not appropriate. In these cases we use slope–area plots to quantify spatial variations in θ, as illustrated for the Danube case study (Section 5.4). We calculate the slope of the main channel using a fixed elevation drop of 5 meters. We wish to look at broad patterns in concavity so we segment the river into reaches based on their geological and/or geographical settings, *e.g.* by sedimentary basin or upland area. In each subjectively defined reach, we apply an iterative Monte Carlo sampling scheme to randomly select 80% of the points within the reach and perform linear regressions to determine a population of θ values for each reach.

5 Concavity across scales

We use the collinearity method outlined in Section 4.1 to investigate concavity across a wide range of different scales, ranging from individual drainage basins to entire mountain ranges. We aim to explore how variable concavity is spatially across different regions and test our ability to constrain a representative θ that can be used in channel steepness calculations.

5.1 Individual drainage basins

As a first step, we illustrate the collinearity method with two small watersheds in different geological contexts (Figure 4). The aim of using D^* is to not only determine the best-fit values for a given watershed, but also to determine how "wrong" other values are. This is necessary because normalized steepness values (k_{sn}) are frequently calculated based on an assumed reference concavity θ_{ref}, which inevitably results in channel steepness values being calculated using values of θ which are inappropriate for an individual basin.

The first example site (Figure 4a,b,c) is in the Loess Plateau (China). It features a relatively homogeneous substrate and relatively homogeneous concavity indices estimated from previous studies (e.g. Mudd et al., 2018; Zhang et al., 2020). The density map in Figure 4a shows D^* values for each value of θ tested, and for each combination of tributaries tested in the watershed. Higher densities (e.g., bright colours) mean that many of the tributary combinations returned that value of D^*. Median values minimising D^* suggest an optimal θ (θ_{opt}) value of 0.425 and a R_θ value of 0.075. A χ–elevation plot made using this concavity (Figure 4b) shows linear channel and tributary profiles, suggesting a channel with homogeneous substrate and a constant erosion rate (Perron & Royden, 2013).

Figure 4c displays transformed river profiles for different θ with a normalised $\chi^* = \chi/\chi_{max}$ to plot the two populations of χ on the same horizontal scale. Both of these θ values lead to substantial divergence from the linear profile in panel **b**. If the θ values in panel **c** were used to determine k_{sn}, one would predict a wide range of channel steepnesses. Low values of θ result in tributaries that have higher values of k_{sn} than the main stem (i.e., they are steeper in χ–elevation space), whereas tributaries have lower values of k_{sn} than the main stem if θ is large. We also observe that the black dataset using $\theta = 0.15$ is closer to collinearity than the red dataset using $\theta = 0.85$ as predicted by its lower disorder value.

The second test site is a watershed located in the South-Eastern Carpathians (the outlet is 5 km NW of Buzau, Romania). The landscape is marked by spatial variations in uplift and subsidence, heterogeneous lithology (Maţenco, 2017, and references therein), and shows strong evidence of stream piracy (e.g. ter Borgh, 2013). Figure 4d presents a density plot of D^* values that feature more scatter than those of the Loess Plateau. However, the most optimal θ_{opt}, which here is 0.275 with a R_θ of 0.15, can still be determined from the minimum value of D^*. Figure 4e demonstrates that the method still isolates the value of θ which maximises collinearity despite prominent breaks-in-slope, a small number of outlier tributaries, and many competing forcings. If we compare the χ–elevation profiles in Figure 4f, we see that the profiles with a high value of θ are much more scattered than those with a low value of θ, which reflects the relative spread of D^* at these θ values depicted in the density plot in Figure 4d.

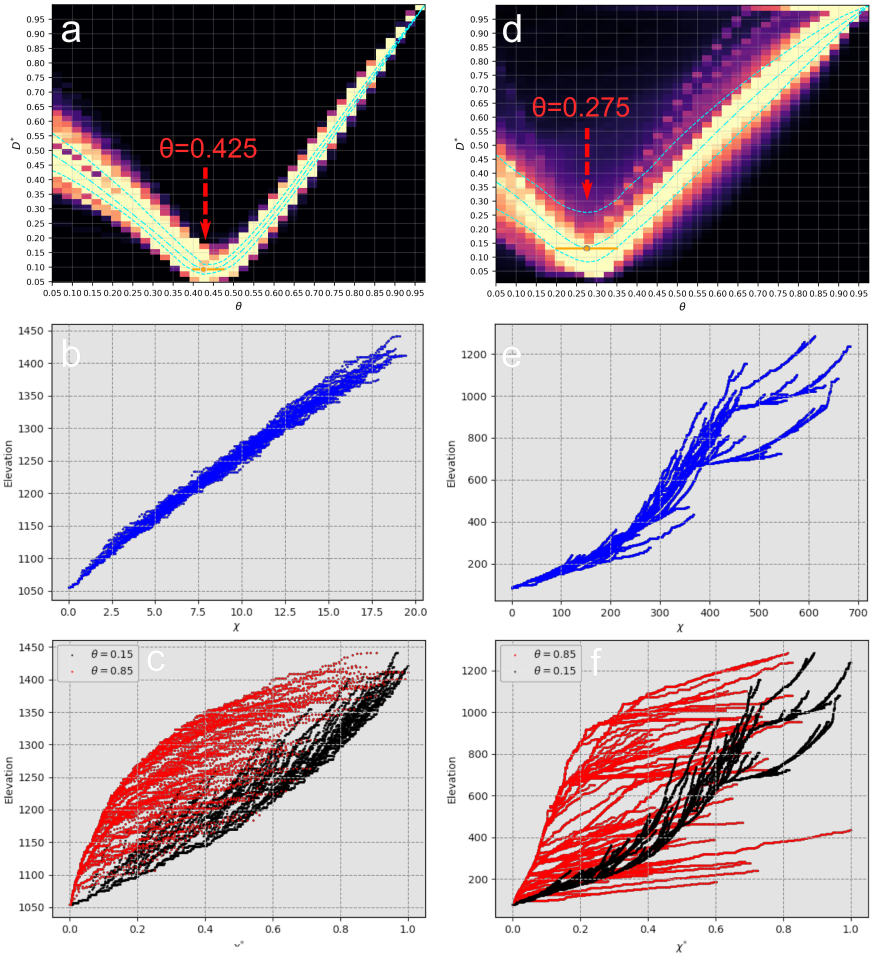

Figure 4. θ best-fit for single watershed in the Loess Plateau (a,b and c) and for the Buzau river (d,e and f) in the South-Eastern Carpathians. a) and d) Density plots of the D^* for each combination of watersheds function of θ. It suggests $\theta_{opt} = 0.425$ and $R_\theta = 0.075$ with a sharp and clear minimum for the Loess Plateau and $\theta_{opt} = 0.275$ $R_\theta = 0.15$ for Buzau. b) and e) χ-Elevation profile for the river at calculated with optimal θ. Note the collinearity of the profiles. c) and f) Nondimensionalised $\chi^* = \chi/\chi_{max}$ calculated with non-optimal θs. Note the high scatter compare to their optimised counterparts.

5.2 Distribution of θ across mountain ranges

A mountain range or discrete upland area is a convenient unit of study in geomorphology (e.g. Gilbert, 1880). To illustrate variations in the concavity index across mountain ranges, we apply our method to a range of sites showing different tectonic and lithological characteristics, as well as a range of scales: The San Gabriel Mountains (CA, USA), the Cordillera Central of Ilocos Norte (Luzon Island, Philippines), the Eastern Carpathians (Ukraine, Romania and Republic of Moldova), and the Himalayas. For each test site, we extract all watersheds within the landscape with drainage areas from 50 km^2 to 1000 km^2. We remove nested watersheds to avoid including the same channels multiple times. This range in drainage area provides a good balance between basins that have a num-

ber of tributaries with which to measure collinearity, and basins having a limited amount of internal heterogeneity such as faults, lithologic contacts or climate gradients.

5.2.1 San Gabriel Mountains

The San Gabriel Mountains sit within the tectonically active Transverse Ranges in Southern California (USA) (e.g. Lindvall & Rubin, 2008). DiBiase et al. (2010) quantified the erosion rates in the area using basin-wide cosmogenic radionuclides and observed positive correlations between erosion rates and k_{sn} in the region. Using linear regressions on binned S–A plots, they suggested θ=0.45. We apply our methodology to the same field area. Figure 5a shows the spatial distribution of most likely values of θ, *i.e* θ value minimising D^* for each basin, across the landscape. A frequency plot of most likely values (Figure 5b) suggests relatively low values of the concavity index with most falling between 0.25 and 0.4 (median is 0.325, and the first and fourth quartile respectively 0.275 and 0.445). Figure 5c shows that more that 60% of the basins have an R_θ below 0.2, meaning their best-fit is narrow and relatively well-defined, with some basins even showing R_θ close to 0.

A strategy to select a representative θ value depends on the watershed of interest. In our case, if we are interested in all the basins on Figure 5, we suggest selecting $\theta = 0.3$ to minimise distortion. This value has been chosen as being one of the most represented, meaning that it will minimise the distorion for a high number of basins, while being very close to the median. Figure 6 can be used to assess which basins will be most disordered, that is, have the highest D^* value for a particular θ value. One might have less confidence in k_{sn} values extracted from basins that are highly disordered in Figure 6 when using the regional θ value.

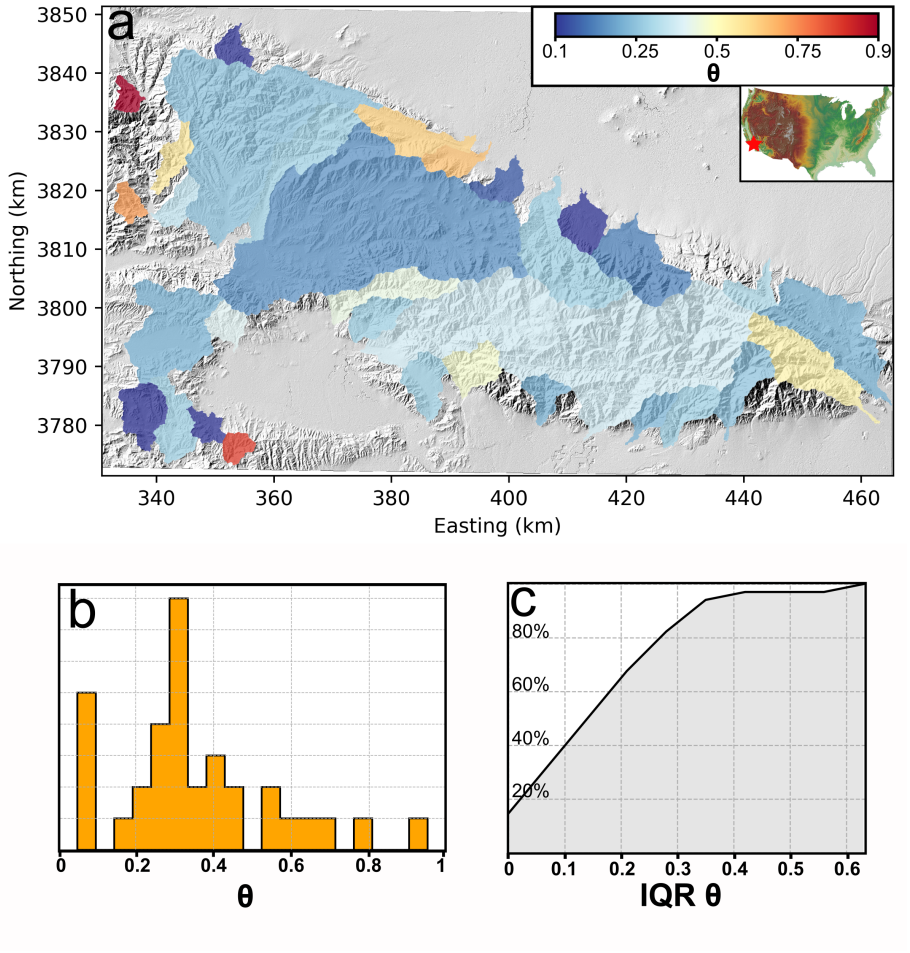

Figure 5. Analysis of the spatial variations in concavity index of the San Gabriel Mountains and surroundings by displaying the distribution of best-fit and their errors. a) Map of best fit θ for each catchment analysed in the area. b) Frequency distribution of the best-fit catchment values. The high concentration of $\theta = 0.05$ is linked to the fact that this is the minimum value considered and encompasses all best-fits lower than this. c) Cumulative distribution plot of R_θ. This plot shows that 80% of the watersheds have R_θ values less than 0.3.

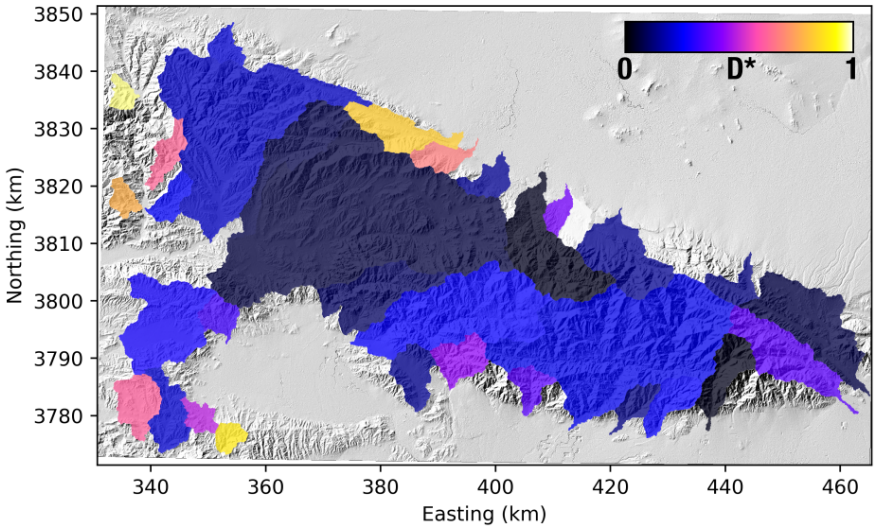

Figure 6. D^* values for each watershed for $\theta = 0.3$. Low values, close to 0, reflect basins that have very low disorder with this value of θ, whereas basins with higher D^* values are much more disordered. Comparison with Figure 5 allows one to identify basins that are highly disordered because they do not share the regional best-fit θ (e.g., the basin in the SE corner of the study area), but it can also identify basins that have a similar best fit θ to the regional value, but are still somewhat disordered (e.g., the basin with an outlet on the southern side of the study area with an Easting of just over 340 km).

5.2.2 Cordillera Central of Ilocos Norte, Philippines

The second test site is the Cordillera Central of Ilocos Norte, in the northern part of Luzon island, Philippines. The island is bordered by doubly vergent subduction zones, one to both the east and west of the island. This tectonic forcing has led to the partition of the island by a network of active faults: the Philippine fault system features shearing, compressive, and extensional faults (e.g. Ringenbach et al., 1992; Aurelio et al., 2009). The analysis of the spatial distribution of concavity indices (Figure 7a) contrasts with the result from the San Gabriel mountains: it is much more heterogeneous. The most occurring value of θ for the range is 0.45 (Figure 7b), but the mountains feature basins with most likely θ values that vary between 0.05 and 0.95, and there is no dominant value or range of values amongst the most likely θ values (Figure 7b).

This heterogeneity is observable from other perspectives: Figure 7c shows the R_θ values of the range. The curve rises much more gradually than that of Figure 5c. Only 40% of the basins have an $R_\theta < 0.2$ and 40% of them have an $R_\theta > 0.4$, suggesting large uncertainties in the most likely value of θ.

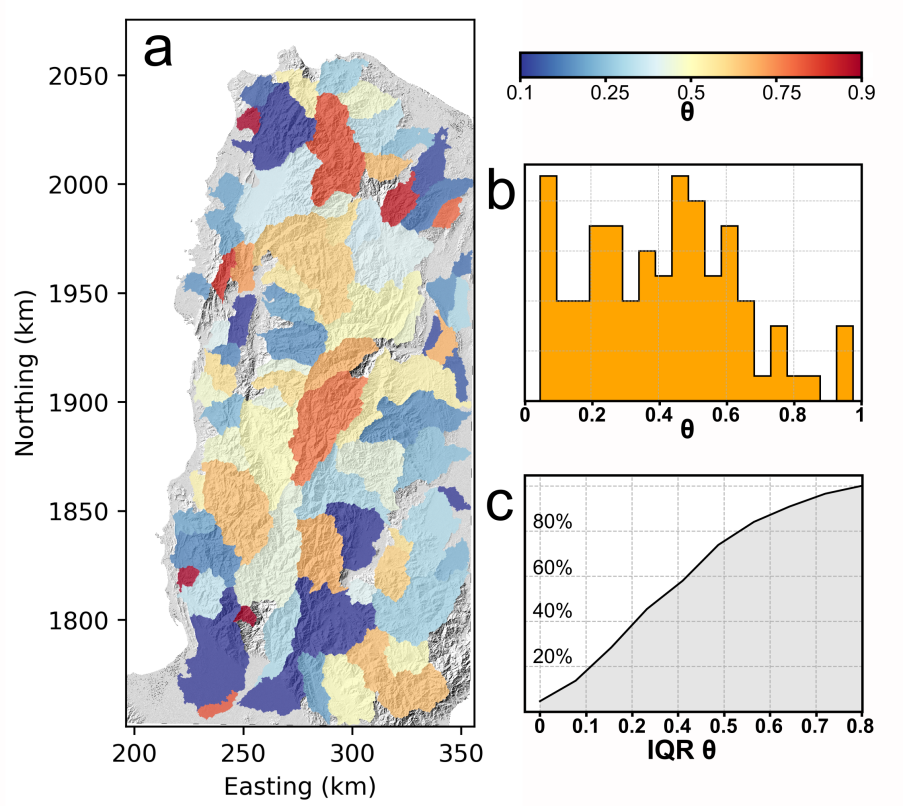

Figure 7. Summary of θ best-fit analysis for Luzon field site (Phillipines). Plots are in UTM zone 51. a) Spatial distribution of the best-fits for each watershed showing striking heterogeneity across the region. b) Distribution of θ values compiled for all watersheds: there is no clear peak in the best-fit θ. c) Cumulative density plot of the uncertainty R_θ. The low steepness of the curve shows the spatial heterogeneity in best-fit θ.

5.2.3 The Eastern Carpathians

The Eastern Carpathians system is part of the eastern continuation of the Alpine orogeny, and is more lithologically heterogeneous than the previous two sites. In their review of the regional tectonics and its topographic expression, Mațenco (2017) (and references therein) highlighted several domains which evolved differently, ultimately controlling emergent features of the topography. The different domains are shown in Figure 8a): (i) the Southern Carpathians, composed of resistant magmatic and metamorphic rocks with the most recent significant exhumation during the Mesozoic; (ii) the Eastern Carpathians, composed of sedimentary rocks of variable strength and fewer magmato-metamorphic massifs, with exhumation history from late Miocene to present in localised sections; (iii) The Transylvanian Basin, an uplifted back-arc basin with potential drainage reorganisation (ter Borgh, 2013); (iv) The Getic and Focsani depressions, made of alluvial fans from the Southern Carpathians and subsidence of the active part of the Eastern Carpathians; and (v) the European Foreland, the foreland basin of the Eastern Carpathians and part of the European Shield (Mațenco, 2017, and references therein).

Figure 8 presents a summary of the concavity index distribution within the Eastern Carpathians. Figure 8b shows the most likely values of θ are widely distributed, but the distribution is centered around 0.625, excluding a large number of values with a best fit of $\theta < 0.05$. Figure 8c suggests that the different domains behave differently. The

Getic and Focsani depressions primarily feature low concavities, between 0.2 and 0.4. Basins in the Southern Carpathians feature low to medium concavity with a wide range of low values between 0.1 and 0.5. The Transylvanian basin and the Eastern Carpathians present similar trends with best-fits centered on 0.5, although the relatively flat distributions suggest a less well constrained best-fit. The European Foreland, in contrast, has high θ values, > 0.6.

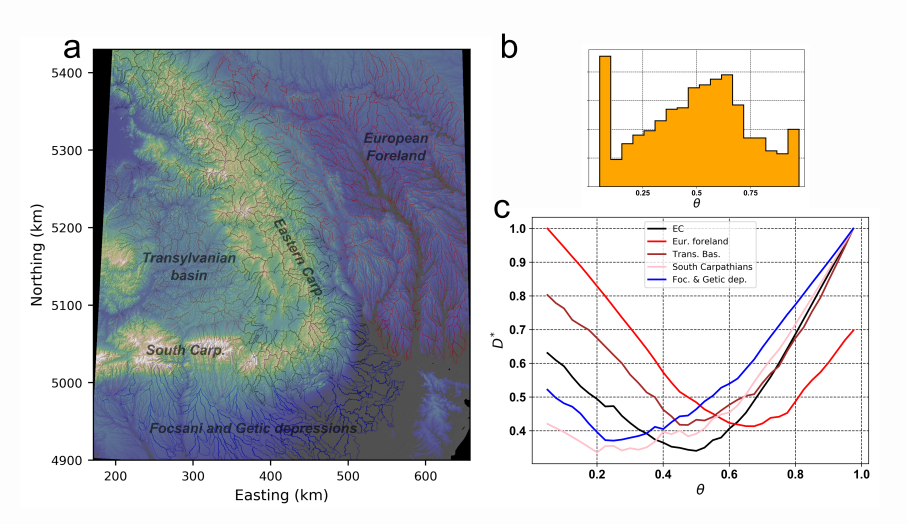

Figure 8. Concavity results from the Eastern Carpathians. a) Watershed between $5e^7$ and $1e^9$ extracted colored by domain corresponding to the legend on c. The base map and subsequent units are in WGS84 UTM35N. b) Best-fit concavity across the field site. Note the peak of low values representing values lesser or equal to 0.05. c) Median profiles of the median D^* for each of the watershed by zones. Global trend can be isolated with significantly different minimums for the different area. The colors correspond to the basin outlined in a) and described in the legend.

5.2.4 The Himalayan system

We also illustrate the spatial distribution of concavity in the central Himalayan system. We include in this analysis the main basins draining the range, outlined in black in Figure 9a, and their surrounding smaller basins on the Tibetan plateau and the Gangetic plain.

Himalayan River networks have been widely studied (e.g. Seeber & Gornitz, 1983; Gupta, 1997; Lavé & Avouac, 2001; Clark et al., 2004), due to the heterogeneous nature of the range's lithology and tectonics (e.g., Yin, 2006), as well as strong gradients in precipitation and discharge (Bookhagen & Burbank, 2010) and the influence of glacial processes on catchment morphology. We find strong variations in θ values (Figure 9). Within the mountain belt, the most likely θ values are centred around 0.45, but large numbers of basins have most likely values between 0.05 to 0.7. Subtle patterns may be recognised; for example the patch of high concavity at Easting 750 km - Northing 3250 km, or the strip of low concavity just north of the basins outlined in black; but apart from systematically low concavity in the plains, no clear signal emerges. This lack of pattern suggests caution should be used in applying a single value of θ across the range when exploring channel steepness.

We also analysed the large scale expression of θ within the major basins, outlined in black, that average the effect of more factors than smaller basins (Figure 9c). Most of the large basins have a global θ in between 0.2 and 0.4 with large uncertainties. One basin features a very high concavity, at odds with Figure 9a, suggesting that large-scale expression of concavity might hide local heterogeneities.

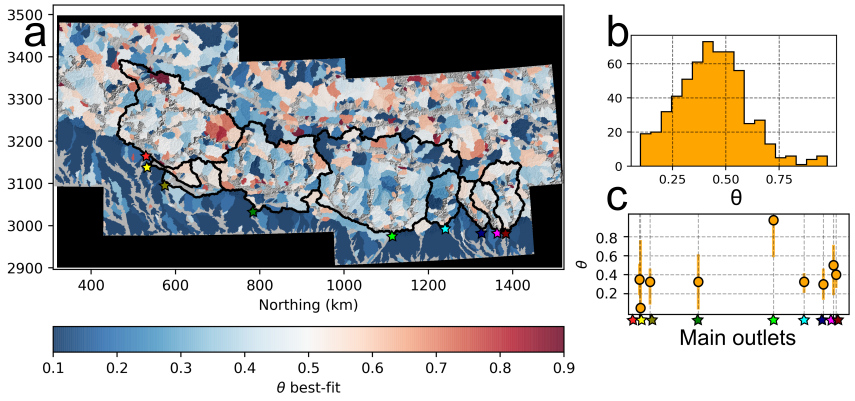

Figure 9. Distribution of θ across the Central Himalaya. a) Spatial distribution of the best-fit θ for all watersheds in a range of drainage area from 50 to 100 km ^{2}. The black outlines are representing the main basins draining to the mountain front. The stars are their outlets and refer to figure c. b) frequency distribution of all the best fits in the study area. Note that the very low values (0.05) have been omitted here for the sake of clarity. c) Best-fit θ for the main drainage basins draining the Himalayas. The outlets are colored on a).

5.3 Variability in the concavity index across multiple basins

To give a broader picture of variation in the value of θ, we analysed θ across many different landscapes, selected to represent a broad range of climate, lithology and tectonic activity.

Our compilation comprises 5033 basins analysed for most likely θ across a diverse range of landscapes. The median value across all these basins is 0.425, which is consistent with previous studies based on slope–area data (e.g. Tucker & Whipple, 2002). This central tendency, however, masks a very large degree of heterogeneity. The interquartile range of most likely θ values is 0.225–0.575. We note that our table makes no effort to isolate bedrock channels, and we may expect greater heterogeneity if the study area includes both alluvial and bedrock rivers (e.g., Whipple, 2004).

The table includes metrics of the range of uncertainties across multiple landscapes. We hope this serves as a benchmark for authors to determine how "messy" their landscape is in a global context. The first and third quartiles for R_θ across all 5033 basins is 0.175 and 0.375, respectively. Therefore, basins with an R_θ value of 0.175 or less have a sharply defined θ compared to most basins, whereas basins with an R_θ above 0.375 are particularly disordered: in these basins it is virtually impossible to constrain a "correct" or representative value of θ based solely on topography.

Table 1. Concavity indices across selected landscapes. At each site we analyse a number of basins and report the median, and first and third quartiles of the most likely θ values amongst the basins. We also report the median and first and third quartiles for the range of uncertainty (R_θ) for individual basins. Maps showing exact locations of study areas and spatial distributions of θ and R_θ can be found in the Supplemental Materials.

Site Name	N Basins	Median θ	Q1 θ	Q3 θ	Median R_θ	Q1 R_θ	Q3 R_θ
Chilean Andes	65	0.475	0.225	0.625	0.275	0.125	0.4
North Arkansas	11	0.65	0.525	0.663	0.3	0.2	0.412
Bureya Massif	75	0.45	0.325	0.55	0.225	0.175	0.325
Eastern Carpathians	876	0.5	0.325	0.65	0.275	0.175	0.375
Caucas Mountains	366	0.362	0.175	0.5	0.25	0.15	0.35
Sierra Madre, Mexico	94	0.45	0.306	0.525	0.25	0.131	0.375
Corsica	30	0.388	0.256	0.425	0.288	0.225	0.444
Ethiopian Highlands	111	0.3	0.2	0.4	0.175	0.125	0.275
Jebal Barez, Iran	54	0.2	0.106	0.275	0.175	0.125	0.25
Lesotho	78	0.475	0.35	0.569	0.175	0.1	0.275
Luzon	88	0.425	0.225	0.575	0.338	0.225	0.475
Edge of Mongolian Plateau	107	0.45	0.35	0.525	0.225	0.125	0.338
Basins along Nujang River	71	0.45	0.325	0.625	0.275	0.175	0.425
Oregon Coast Ranges	26	0.538	0.338	0.75	0.25	0.175	0.3
San Gabriel Mountains	34	0.325	0.275	0.444	0.212	0.125	0.3
Southern Altai Mountains	551	0.35	0.175	0.525	0.25	0.15	0.4
Southern Brazil	102	0.475	0.4	0.55	0.225	0.15	0.275
Western South Africa	634	0.25	0.125	0.425	0.225	0.15	0.35
Southern Wisconsin	60	0.562	0.45	0.625	0.2	0.144	0.325
Yemen	52	0.4	0.275	0.506	0.175	0.125	0.256
Atlas Mountains	26	0.4	0.275	0.5	0.225	0.175	0.325
Dolomites	28	0.538	0.35	0.756	0.338	0.225	0.5
Hida Mountains	51	0.5	0.3	0.575	0.3	0.225	0.438
Himalayas	645	0.4	0.25	0.525	0.275	0.175	0.4
Allegheny Plateau	118	0.7	0.556	0.819	0.25	0.175	0.394
Northern Appalachians, USA	177	0.525	0.4	0.675	0.35	0.225	0.45
Southern Appalachians, USA	277	0.5	0.3	0.625	0.35	0.225	0.45
Olympic Mountains	33	0.575	0.4	0.675	0.325	0.2	0.425
Pyrenees	61	0.475	0.3	0.575	0.325	0.225	0.4
Taiwan	97	0.45	0.15	0.575	0.275	0.2	0.375
Tien Shan	40	0.612	0.5	0.756	0.325	0.25	0.481
Zagros Mountains	49	0.475	0.3	0.625	0.25	0.125	0.4

5.4 Variability along continental-scale rivers: the Danube

Our previous test sites aimed to show the variation of concavity across different scales of field site. However there is still a particular case that has not been investigated: continental-scale rivers. Here we do not aim to extract concavity values over sets of basins, but rather over a large river crossing a continent. Exploring θ over a large river is particularly important for χ, because the χ coordinate integrates discharge data from base-level to top. Thus, χ values at basin headwaters are sensitive to poorly fit values of θ downstream (Forte & Whipple, 2018).

The Danube is the second longest river in Europe which flows for approximately 2,860 km, connecting the Alps to the Black Sea. It acts as a major source-to-sink component of the Alpine-Pannonian-Getic-Black-sea system and sets boundary condition for the erosion of the North-Eastern Alps (Matenco et al., 2013). It also crosses several sedimentary basins which are separated by gateways, each having a history of opening and closing through geological time (e.g. Leever et al., 2010, 2011).

We extracted the Danube river long profile using a pre-conditioned DEM from the HydroShed (Lehner et al., 2008), and segmented the profile by very general domains: i) the Danube delta and crossing of the Northern Dobruja range (Eastern Romania, in dark blue in figure 10); ii) the Dacic depression, foreland of the South Carpathians (light blue in figure 10); (iii) the Iron Gates, the gateway between the Dacic depression and the Pannonian Basin (green in figure 10); (iv) the Pannonian Basin (orange in figure 10) and the Alpine Danube (red on figure 10). Processing of concavity along the river suggest systematically low concavity on most of the sedimentary basins (between -0.15 and 0.15). The Iron gate area and the Alpine Danube show higher concavity around 0.3.

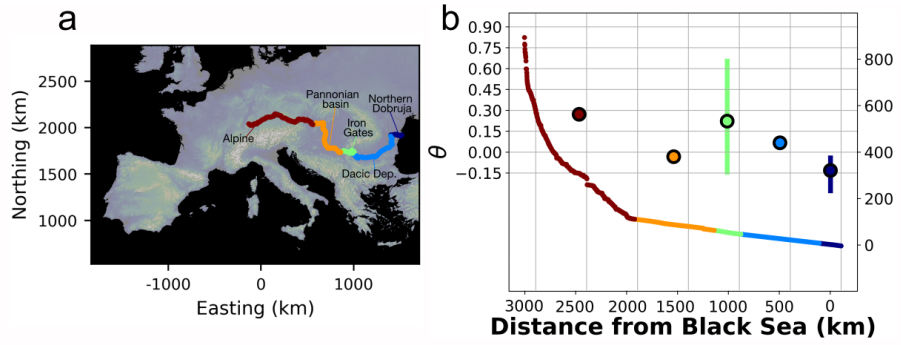

Figure 10. a) Map of the Danube River's course, coloured by domains discussed in the text. Raster preconditioned by Hydroshed (Lehner et al., 2008) and projected in Lambert Conformal Conic. b) Long profile of the Danube river, with θ for each river domain. Note the overall low concavity on θ for most of the lowlands.

6 Distortion of k_{sn} and χ values linked to variations in θ

We have demonstrated the variability of θ values at a wide range of scales. When studying a field site, no matter the scale of the area, one needs to assume a reference θ_{ref} for the study in order to use k_{sn} or χ. This forces the worker to calculate k_{sn} with θ values that may not be the most likely for some of the watersheds. Therefore, we now move on to explore how changing values of θ will distort k_{sn} and χ values, and consequently our interpretation of landscape metrics. We first investigate analytical expressions of the distortion, and then illustrate the distortion using real landscapes.

6.1 Distortion of k_{sn}

Interpreting k_{sn} in a meaningful manner involves focusing on the contrasts between slope patches, *sensu* Royden and Perron (2013) across a field site. Indeed, local contrasts in k_{sn}, *i.e.* a knickpoint, are commonly interpreted as driven by phenomenon such as climatically driven base-level drop (e.g. Crosby & Whipple, 2006; ?, ?; Prince & Spotila, 2013) or tectonically-driven changes in uplift or fault throw rates (e.g. Kirby & Whipple, 2012; Whittaker & Boulton, 2012; DeLong et al., 2017; Mitchell & Yanites, 2019; Struth et al., 2019). If contrasts between two slope patches are exaggerated, attenuated, inverted, annihilated or artificially created, spurious patterns carry a real risk for misinterpretation.

6.1.1 Analytical formulation of k_{sn} distortion

We consider two points in a channel network, labelled with subscripts M and N, that are characterised by their slope and drainage area (S_M, A_M) and (S_N, A_N). Their k_{sn} values (expressed as k_M and k_N can be expressed rearranging equation 1 as follows:

$$k_M = S_M {A_M}^{\theta_{ref}} \tag{14}$$

and

$$k_N = S_N {A_N}^{\theta_{ref}} \tag{15}$$

We can calculate the ratio of k_{sn} for these data points, which we call r_k, that is valid for a given θ:

$$r_{k,\theta} = \frac{S_M {A_M}^{\theta}}{S_N {A_N}^{\theta}} \tag{16}$$

Which we recast with a slope ratio, r_S, and an area ratio, r_A:

$$r_{k,\theta} = r_S \, {r_A}^{\theta} \tag{17}$$

Where $r_S = \frac{S_M}{S_N}$ and $r_A = \frac{A_M}{A_N}$. To assess the distortion linked to changing the value of θ, we aim to express the ratio r_k as a function of $\Delta\theta$, with $\Delta\theta$ defined as:

$$\Delta\theta = \theta_2 - \theta_1 \tag{18}$$

with θ_1 and θ_2 are the different concavities used. A logarithmic transformation can simplify comparison of k_{sn} values for different values of θ at sites M and N:

$$\ln[r_{k,\theta_2}] - \ln[r_{k,\theta_1}] = \ln[r_S] + \theta_2 \ln[r_A] - \ln[r_S] - \theta_1 \ln[r_A] \tag{19}$$

The slope ratios cancel because these are not affected by θ:

$$\ln[r_{k,\theta_2}] - \ln[r_{k,\theta_1}] = \Delta\theta \ln[r_A] \tag{20}$$

We can define a factor that quantifies the distortion ratio between the two k_{sn} values as we vary θ, which we call the distortion factor, β_r:

$$\beta_r(\Delta\theta) = \frac{r_{k,\theta_2}}{r_{k,\theta_1}} = r_A^{\Delta\theta} \tag{21}$$

The distortion factor $\beta_r(\Delta\theta)$ represents a ratio of the differences in k_{sn} at two fixed points in the channel network for two different values of concavity θ, thus reflecting how sensitive gradients in k_{sn} are to the use of different values of concavity θ. Higher values of β_r reflect greater distortion of k_{sn}, meaning that changing θ values will have a greater impact on the interpretations of spatial variations in k_{sn}.

6.1.2 Examples of k_{sn} distortion in real landscapes

We first illustrate distortion of k_{sn} with the test sites used in Figure 4. Figure 11 shows the extent of k_{sn} distortion for different hypothetical cases where θ is set at a value that differs from the most likely value. We normalise all the k_{sn} values by their range of values, noted k^*_{sn}, to circumvent the differences in magnitude between the different values of θ. We display their median basin-wide distribution, binned by distance from their respective outlets.

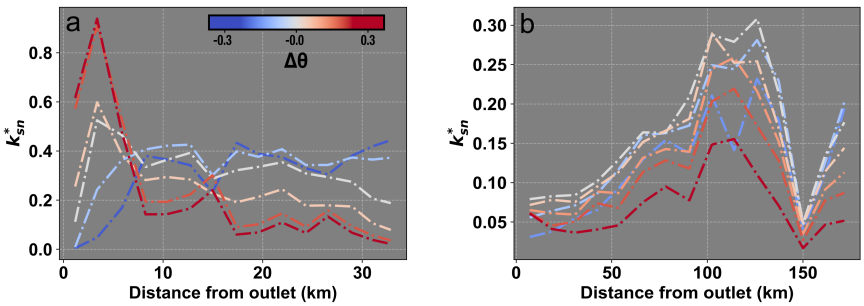

Figure 11. a) Distribution of k^*_{sn} – *i.e.* normalised to range – for a range of θ along the watershed investigated in section 5.1a) (Loess Plateau, People's Republic of China). The different colours correspond to $\Delta\theta$ from the best fit $\theta = 0.425$. b) Distribution of k^*_{sn} for a range of θ along the watershed investigated in section 5.1d) (Buzau river, Romania). The different colours correspond to $\Delta\theta$ from the best fit $\theta = 0.275$.

Figure 11 gives an insight of the possible distortion at the scale of a single watershed. At optimal $\theta_{opt} = 0.425$ for the first field site (see section 5.1), figure 11a depicts a k_{sn} profile showing an initial increase of k_{sn} in the first 8 kilometres followed by a slight decrease in median value the rest of the profile. Using $\theta > \theta_{opt}$ gradually inverts this contrast by over-estimating k_{sn} in the first section of the profile. The normally decreasing part of the profile is gradually over-estimated. On the other hand, using $\theta < \theta_{opt}$ exaggerates the contrast between the lowest values near the outlet and the rest of the profile. The slightly decreasing pattern becomes flat or even increasing for very low θ.

The second and more heterogeneous field site (Buzau, Romania, see section 5.1, $\theta_{opt} = 0.275$), shows a gradual increase of k_{sn} followed by a sharp decrease near the headwaters of the network (figure 11b). Changing the value of θ at this site does not change the overall pattern of channel steepness, however overestimates of θ result in a flattening of the contrasts.

We also extracted illustrative k_{sn} distortion across multiple basins within the Luzon field site (Figure 12, see Section 6 for context). A number of potentially spurious patterns emerge with the use of different θ values to calculate k_{sn}.

In this site, higher values of θ result in the largest proportion of high values of steepness in the range. The zone of high k_{sn} values in Figure 12c is more extensive than the one in Figure 12a. Another systematic observation at higher θ, is that channels with more drainage areas feature higher values. We determined an area of interest outlined in light green (to not interact with the k_{sn} color scheme) in Figure 12a, b and c in order to illustrate more thoroughly some aspects of the distortion.

The green area includes a number of sub-basins draining to a low-relief area. At $\theta = 0.2$, the larger channels have low steepness values, and the northern section of the range has generally higher k_{sn} than the eastern section of the range. The plain has systematically low steepness and no sharp contrasts in k_{sn} are visible. When $\theta = 0.45$, river steepnesses increases. Contrasts between the different sections are less pronounced but a few steeper areas do appear. At $\theta = 0.7$, some of the larger rivers become steeper than the surrounding terrain. A number of sharp k_{sn} patches appear.

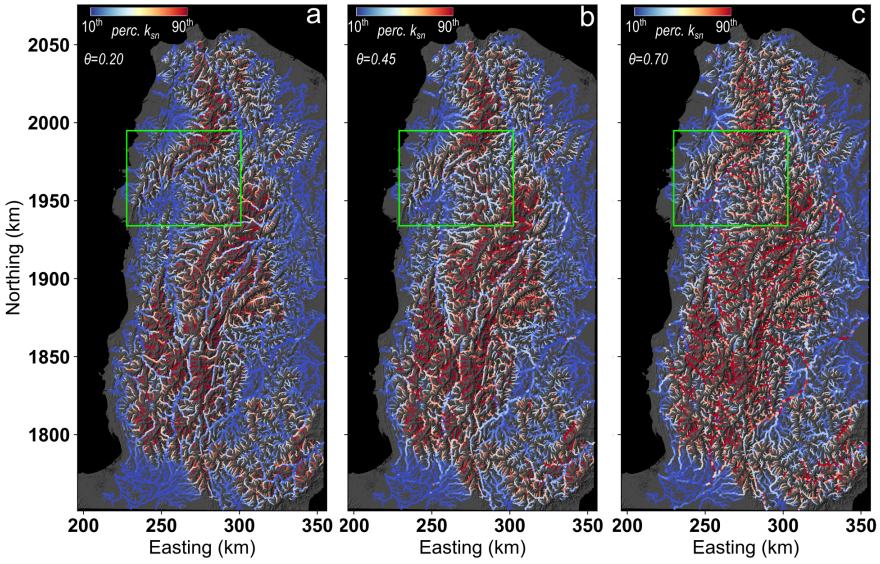

Figure 12. River network in the Luzon island (Philippines) coloured by k_{sn} values for different θ. In order to produce comparable results, the minimum and maximum colours are set to respectively the 10^{th} and the 90^{th} percentile of each k_{sn} populations. θ values have been picked in order to represent the general distribution of best-fits (see Figure 7): 0.20 for a), 0.45 for b) and 0.70 for c). River points are sized by $log[A]$ and largest A are plotted on top.

6.1.3 Subsequent implications and predictions

Equation 21 highlights a number potential biases in k_{sn} values when calculated with non-optimal θ. Figure 13 presents the analytical solution to the distortion β_r, which has the amusing property of looking like a bow tie.

Interpreting this bow tie may be slightly confusing, since β_r is a ratio of ratios. Let us let first give a more concrete example: consider a landscape where, at a given value

of θ all the values of k_{sn} are the same. This means that r_{k,θ_1} must always equal unity and that β_r will be equal to the ratio in channel steepness between two points with a drainage area threshold r_A. If the θ value is reduced, then channel reaches with a larger drainage area will have a smaller k_s value than those with smaller drainage area. If the θ value is increased, then it is the reaches with larger drainage area that will increase their k_s values relative to smaller channels.

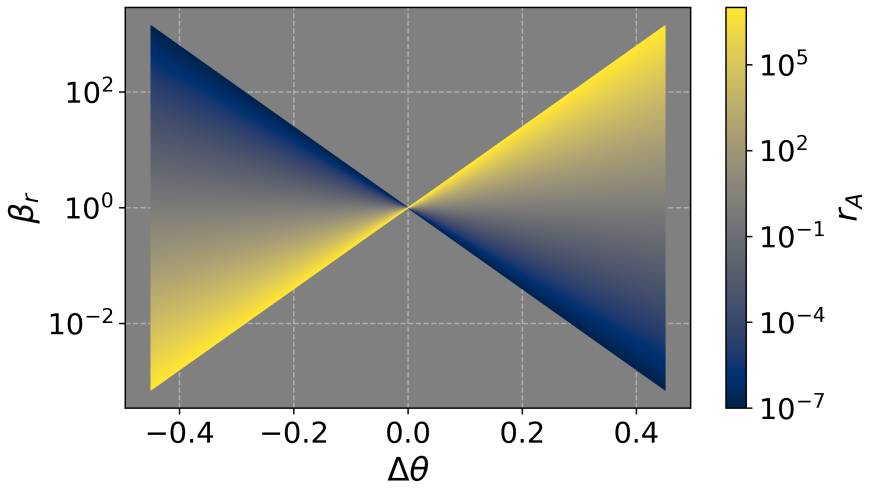

Figure 13. The distortion ratio (β_r) as a function of the change in θ, colored by the ratio of drainage area between two points.

Having highlighted the most basic feature of Figure 13, we can expand upon the nature of distortion, which is a function of (i) how different the local θ is from the global best fit and (ii) the differences in drainage area amongst the compared channel reaches.

To illustrate this behavior, consider two slope patches, (sensu Royden & Perron, 2013), with a contrast in k_{sn} of r_k and a contrast in drainage area r_A. Several scenarios can be considered which relate to potential distortion of k_{sn} patterns in real landscapes.

First, assume that these two slope patches are contiguous, within the same river and without any significant tributary joining between them (i.e., they will have similar drainage areas). Their r_A will typically be very low, *e.g.* between 0.9 and 1.1, depending on the source dataset and local context. As illustrated in Figure 13, distortion for a low ratio of drainage areas is insignificant, with a distortion of the ratio in the order of 1.05 in the worst cases. It suggests using non-optimal θ will not impact the importance of local knickpoints, relative to their immediate surroundings.

This might give one confidence that we do not need to worry about distortion when identifying knickpoints based on k_{sn} data. However, many studies base interpretation of factors driving the presence of knickpoints by their spatial distribution (e.g. Crosby & Whipple, 2006; Whittaker & Boulton, 2012; Mitchell & Yanites, 2019). Because river channels feature many fluctuations in gradient, simply looking for changes in k_{sn} may result in large numbers of potential knickpoints (e.g. Gailleton et al., 2019), so we must compare the relative magnitude of knickpoints in different channels, which will inevitably have different drainage areas. In this case distortion due to non-optimal θ becomes problematic. If we consider two knickpoints having the same Δk_{sn} contrast if the most likely

θ is used (i.e., $\Delta\theta = 0$), but one of these is in a small tributary (*e.g.* $1e^5m^2$) and another one in the more prominent channel (*e.g.* $1e^9m^2$, r_A in the order of $1e4$), the distortion β_r can rapidly rise up to 20 times higher/lower depending on the $\delta\theta$. This confirms earlier observations from topographic analysis suggesting the location of contrasts in k_{sn} does not move with different values of θ but their relative importance would be modified (Gailleton et al., 2019).

Next, consider two slope patches of differing drainage area located within the same watershed. This can represent a wide range of possible scenarios in real landscapes, for example contiguous slope patches up and downstream of a tributary junction, slope patches on different rivers, or slope patches on the same river that lie some distance from each other. The resulting distortion from varying the θ value can either generate new contrasts, erase existing ones or even invert the steepness signals (Figure 13), as observed in the Loess Plateau in section 6.1.2. For example, a point with lower k_{sn} in the main river relative to a tributary will see the contrast between the two shrink with potential inversion of the two values if the θ value is increased (i.e., $\Delta\theta > 0$). On the other hand, the ratio of k_{sn} will grow exponentially larger with $\Delta\theta < 0$. The exact nature of the distortion is case specific when it comes to changes in drainage area and needs to be considered carefully. Figure 13 can be used, along with constraints on θ, to assess the risk of distortion for particular cases. Figure 13 also shows that the key parameter in determining the degree of distortion is the drainage area.

6.2 Influence of concavity values on the distortion of the χ coordinate

6.2.1 Analytical formulation of χ distortion

Expressing the analytical distortion of χ linked to varying concavity is less straightforward than for k_{sn}, which is solely defined by constant S and A values. The χ coordinate at a given point x of the river profile, is dependent on the downstream river network and tributaries as it integrates $(A_0/A(x))^\theta$ from the outlet to x. This has two direct consequences.

First, the χ value depends on the location of base level, x_0. This issue is out of the scope of the present study and has been thoroughly discussed in multiple studies (e.g. Forte & Whipple, 2018; Seagren & Schoenbohm, 2019). We direct the interested reader to Figure 2 in Forte and Whipple (2018) for an illustration of the significant impact of base level choice on χ contrasts.

Secondly, solving for distortion requires constraining the downstream shape of the river network. However, river flow distance x as a function of drainage area varies from river to another. For an analytical solution, we use an approximation by expressing the distance from the outlet, x, as a function of drainage area, A:

$$A(x) = (X_0 - x)^\rho \tag{22}$$

where X_0 is the maximum distance of the river to the outlet (*i.e.* the distance from the source to the chosen base level), and ρ a positive exponent approximating the rate at which drainage area decreases toward the headwaters. This is a variation of Hack's law (Hack, 1957), as Hack's law described A as a function of flow distance downstream. Although very simplified, equation 22 can simulate realistic drainage area distribution along river profiles. We can then use the standard definition of the χ coordinate (e.g. Perron & Royden, 2013):

$$\chi(x) = \int_{x_b}^{x} \left[\frac{A_0}{(X_0 - x)^{-\rho}} \right]^\theta dx \tag{23}$$

Integrated, this becomes

$$\chi(x) = \frac{A_0^\theta (X_0 - x)^{(1-\rho\theta)}}{\rho\theta - 1} - \frac{A_0^\theta (X_0 - x_b)^{(1-\rho\theta)}}{\rho\theta - 1} \tag{24}$$

By definition, the outlet, x_b, has a coordinate of 0 (x is defined as the distance from the outlet), so inserting this we arrive at:

$$\chi = -\frac{A_0^\theta}{\rho\theta - 1} \left[(X_0 - x)^{(1-\rho\theta)} - X_0^{(1-\rho\theta)} \right] \tag{25}$$

Willett et al. (2014) suggested that differences in the χ coordinate across drainage divides indicated disequilibrium in tectonic forcing and that drainage divides would migrate away from the side of the divide with a lower χ value. Conversely, if the χ value is the same on either side of the divide for two points with the same elevation, then the divide should be stable.

We can explore the impact of changing θ on the χ coordinate on either side of the divide if we further simplify equation 27 by setting $A_0 = 1$ m^2 (this is the value chosen in most studies). In addition, the χ coordinate used to evaluate differences across divides is typically extracted at a critical drainage area (A_c) (e.g. Willett et al., 2014; Forte & Whipple, 2018). We can calculate the distance from the outlet of this critical drainage area from equation 22:

$$x_c = X_0 - {A_c}^{1/\rho} \tag{26}$$

Inserting equation 26 into equation 27 and setting $A_0 = 1$ m^2, we arrive at:

$$\chi_d = -\frac{1}{\rho\theta - 1} \left({A_c}^{1/\rho - \theta} - X_0^{(1-\rho\theta)} \right) \tag{27}$$

Now consider two points on either side of a divide with the same elevation and the same χ coordinate. The basins on either side of the divide could have different topology, so could have different values of ρ and different values of X_0. If we call these values in the second catchment ρ_1 and X_1, we can fix the two χ coordinates to the same value:

$$\frac{1}{\rho\theta - 1} \left({A_c}^{1/\rho - \theta} - X_0^{(1-\rho\theta)} \right) = \frac{1}{\rho_1\theta - 1} \left({A_c}^{1/\rho_1 - \theta} - X_1^{(1-\rho_1\theta)} \right) \tag{28}$$

If we assign the value of X_1, we can solve equation 28 for ρ_1.

Using these values of ρ, X_0, ρ_1, and X_1 from basins that have the same value of χ at a critical drainage area of A_c, and which we have defined as being at equilibrium so therefore having the same elevation at these points, we can then alter the value of θ by some offset, $\Delta\theta$. When θ is modified, the χ coordinate will change in each basin. But the two new χ values will not be the same, generating an difference in χ at the divide that is an artefact of choosing an incorrect value of θ.

We find that the offset in χ at the divide caused by selecting an incorrect value of θ is most sensitive to the correct value of θ, the value of $\Delta\theta$, and the ratio between the lengths of the basins that share a divide, X_1/X_0. We plot results as the percent offset in χ at the divide, which under some parameter values can exceed 40% (Figure 14).

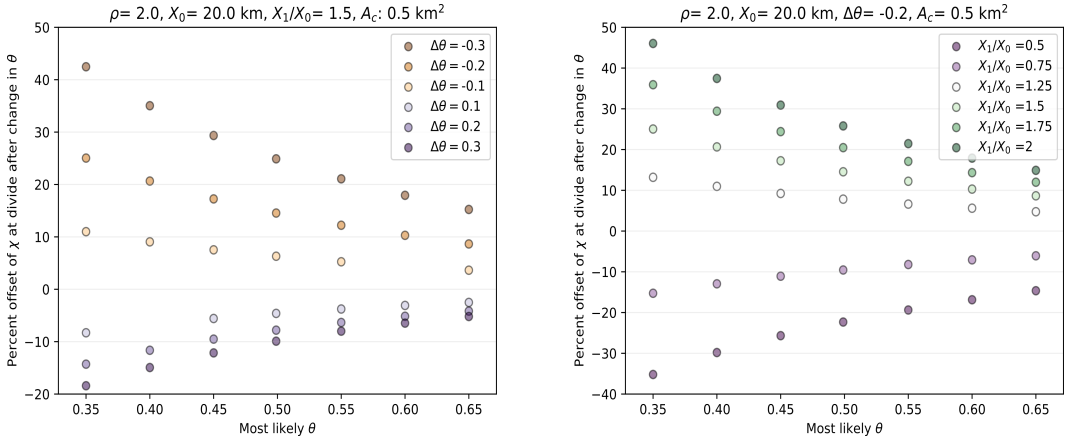

Figure 14. Percent difference in the χ coordinate for two basins whose χ values are the same for one value of θ, but are different lengths (X_0 and X_1), resulting in distortion of the χ coordinate when θ is changed by $\Delta\theta$. In the left panel, we show the sensitivity to $\Delta\theta$ whereas we show the sensitivity to the difference in length between the two catchments.

Spurious offsets in χ at the divide are greater when the correct value of θ is smaller. Unsurprisingly, offsets are greater for greater values of $\Delta\theta$. The value of χ is greater in the longer catchment if θ has been overestimated (e.g., $\Delta\theta < 0$). In the nomenclature of Willett et al. (2014), if θ has been overestimated, the shorter basin will spuriously appear to be the aggressor. We have shown in Section 5.3 that most likely values of θ can vary substantially from the central value of 0.45. If the most likely value is high, such as in the Allegheny Plateau or in the Ukraine (Table 5.3), the distortion for choosing a concavity index of 0.45 will result in relatively small distortions of around 10%, but the errors will be much larger in locations with low concavity values if a θ value of 0.45 is used. We should remind the reader that our analytical examples use the rudimentary approximation of the relationship between length and area described by equation 22, so we now move on to examples in real catchments.

6.2.2 Illustration of χ distortion in real landscapes

We select 3 sites in different geographical and geological contexts to explore the ratio of χ values across selected divides for a range of θ values. Figure 15 presents the results for the three test sites. The first site (Figure 15a and d) is the island of Puerto Rico (United States of America), which is subject to differential climatic, tectonic and lithologic forcings (e.g. Pike et al., 2010). The island does feature a common base level of the Atlantic ocean as well as asymmetric river lengths on both side of the divide. The second site (Figure 15b and e) is located in the Loess Plateau (People's Republic of China); the site described in Section 5.1 lies within this area. We fix the base level at the Wei River, close to the relief front and at similar elevation. Finally we explore the Carpathian Mountain Range (Figure 15c and f) and the main divide across the Eastern and South Eastern Carpathians, with calculation of χ using the Black Sea as base level. For the sake of readability, we chose to display the maps with the widely used $\theta = 0.45$ and the θ tested are 0.05, 0.25, 0.45, 0.65, 0.85.

Puerto Rico's cross-divide χ–ratios show wide variations across theta values (Figure 15). Values of χ tend to be higher on the northern side of the divide (note rotation of figure).

The analytical solutions (Figure 14) suggest that reducing the value of θ will result in longer catchments having greater values of χ at the divide. This is illustrated in Figure 15d, where very large differences in χ at the divide are seen for low values of θ at a divide distance of $\approx$ 150 km, which is where the difference in length of the northern and southern catchments is the greatest. Changing χ values caused by changing values of θ can even lead to inversion of the side of the divide with greater χ, for example at a distance of approximately 12 km along the divide, where, when θ is low the northern catchments have greater χ but when θ is high it is the southern catchments with greater χ values.

The Loess Plateau's cross-divide χ–ratio at $\theta = 0.45$ suggests a relatively stable contrast across the area, consistent with previous findings (Willett et al., 2014). The two basins on either side of the divide have a most likely θ value of 0.4, very close to $\theta = 0.45$. The absence of large changes in the offset of χ across the divide for different values of θ in comparison to the other two study sites is also consistent with the analytical solutions: the basins on either side of the divide feature similar distances between base level and the divide. In this landscape it seems that selecting a value of θ inconsistent with the most likely value of θ would not have a large impact on the χ offset at the divide. However if χ is used to derive k_{sn}, the same distortion as the previous section are expected to occur.

The third test site in the Carpathians is the largest of the three and the most heterogeneous: the χ calculation encompasses the entire whole mountain range and major sedimentary basins with very low relief as described in Section 5.4. The rivers on the southern and eastern side of the divide are linked more closely, in terms of flow distance, to the Black Sea whereas the rivers on the Western side of the divide travel around the Southern Carpathians through the Pannonian basin, flowing along the Danube and Olt rivers. As shown in the section investigating the spatial variations in θ in the region, the most likely values of θ are very heterogeneous. The patterns at the start and at the end of the divide profile are inverted when switching from low to high θ.

Again, we can use the analytical solutions to inform these results. At the southern section of the divide, the western basin flows along the Olt river, which we can see in Figure 15c dissecting the southern Carpathians, leading to a relatively modest difference in flow length across the divide. In the center of the divide, the basins on the western side of the divide flow a much greater distance, and so for decreasing values of θ the difference of χ across the divide grows much greater, to values on the west more than 3.5 times those on the east.

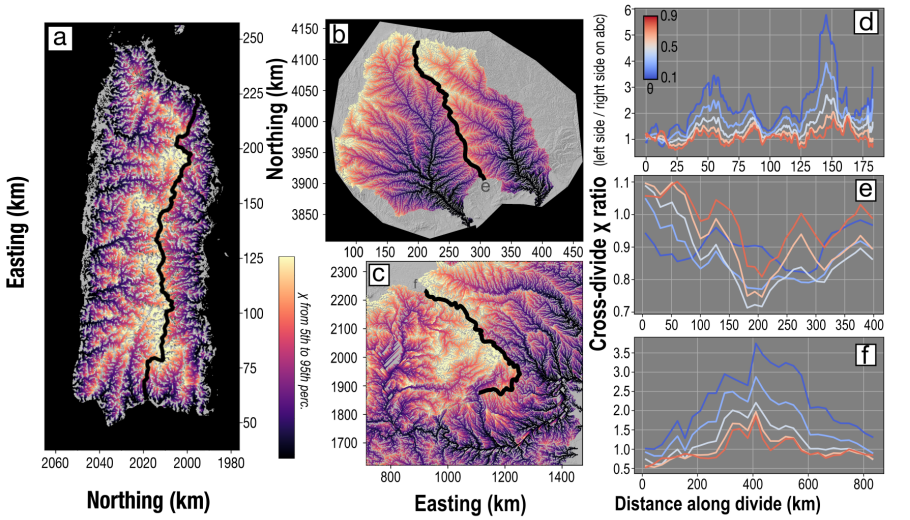

Figure 15. Illustration of χ distortion effect on real landscapes. a) b) and c) show the χ map at $\theta = 0.45$ for respectively Puerto Rico (WGS84-UTM19N), Loess Plateau (People's Republic of China) and the Carpathians-Pannonian-Black Sea are (Czech Republic, Slovakia, Hungary, Romania, Bulgaria, Ukraine, Moldova, Poland, Serbia). χ color scheme is based on the 5^{th} to the 95^{th} percentile for each of the respective maps. the investigated divides are displayed in bold black lines. d), e) and f) shows the cross divide for the three respective field sites. The ratio is calculated for a window of 5 km across divide for Puerto Rico and 40 km for the others.

7 Conclusions

In this contribution, we expanded methods to determine most likely value of the concavity index, θ, using disorder metrics (e.g. Goren et al., 2014; Hergarten et al., 2016; Mudd et al., 2018; Shelef et al., 2018) that quantify both the uncertainties in θ and the degree to which changes from the most likely value of θ affect the overall disorder of the channel network. Because determination of normalized channel steepness index k_{sn} requires the assignment of a reference value of θ, these metrics can give the user insight into the degree to which each basin is likely distorted by a θ value that differs from its most likely value in a particular basin.

We go on to explore variation in most likely θ values across numerous catchments using the disorder metric. This mirrors earlier studies which aimed to constrain θ using S–A methods (Tucker & Whipple, 2002). Our results indicate that θ values have a central tendency of 0.425 similar to that suggested previously from S–A analysis (e.g., Whipple et al., 2013, and references therein). The first and third quartiles across 5033 basins are 0.225 and 0.575. Given this range, we suggest authors should never assume a reference value of θ without testing for the most likely values.

As fixing a reference θ will result in calculating k_{sn} using a θ value that is not the most likely value for each basin, we assessed, both analytically and numerically, the extent to which selection of θ distorts k_{sn}. When comparing values from different points in the channel network, the contrast in drainage area and $|\Delta\theta|$ controls the magnitude of the distortion, which can reach several order of magnitudes. We demonstrate that changing θ can change the spatial distribution of k_{sn}, leading to the risk of misinterpretation of uplift or erosion signals. We also find that existing contrasts between areas of high and low k_{sn} can be inverted or erased. On the other hand, local adjacent contrasts are

are not affected if no tributary junction separate them, meaning that detection of knickpoints is unlikely to be affected by changing θ.

We have not explored strategies to circumvent spatially varying θ in k_{sn} studies, but can speculate on possible approaches based on our analyses of the spatial variance of θ across a wide range of landscapes. One approach would be to non-dimentionalize k_{sn} using, for example, a statistical representation of its distribution. Another approach, if one is studying a large enough landscape, is to compare populations of basins that share the same most likely value of θ. Finally, one could simply reject analysis of basins with outlying most likely θ values.

We also investigated how χ values evaluated across divides are affected by changes in θ. Differences in the χ coordinate have been used as a proxy for drainage divide migration (e.g. Willett et al., 2014), so if the difference in χ across the divide is affected by changes to θ there is a risk of misinterpreting the presence or absence of divide migration. We first explored simple analytical solution of χ distortion across a divide and found that basins with lower values of θ were more sensitive to χ distortion. One key control is the length to base level of basins on either side of the divide. We find that for lower values of θ, longer basins will have increasing χ values, so reductions in θ will can result in longer basins being spuriously interpreted as "victims" catchments using the nomenclature of (Willett et al., 2014). Applications on real landscapes suggested that at spatially constant θ, the basins interpreted as aggressors were rarely inverted across drainage divides, but the magnitude of the χ offset varied by, in some cases, a factor of 3 with large changes in θ. This implies that it can be extremely challenging to robustly compare the χ coordinate across divides in locations with spatially varying θ.

Acknowledgments

This project has received funding from the European Union's EU Framework Programme for Research and Innovation Horizon 2020 under Grant Agreement No 674899 (Subitop). This research utilised Queen Mary's Apocrita HPC facility, supported by QMUL Research-IT. http://doi.org/10.5281/zenodo.438045

References

Aurelio, M. A., Galapon, J. B., Hizon, V. T., & Sadsad, D. B. (2009, mar). Stress behavior from fault data sets within a transtensional zone, South Central Cordillera, Luzon, Philippines: Implications for mineral occurrences. *Island Arc*, *18*(1), 144–154. doi: 10.1111/j.1440-1738.2009.00661.x

Bookhagen, B., & Burbank, D. W. (2010). Toward a complete Himalayan hydrological budget: Spatiotemporal distribution of snowmelt and rainfall and their impact on river discharge. *Journal of Geophysical Research: Earth Surface*, *115*(F3).

Clark, M. K., Schoenbohm, L. M., Royden, L. H., Whipple, K. X., Burchfiel, B. C., Zhang, X., ... Chen, L. (2004). Surface uplift, tectonics, and erosion of eastern Tibet from large-scale drainage patterns. *Tectonics*, *23*(1).

Crosby, B. T., & Whipple, K. X. (2006). Knickpoint initiation and distribution within fluvial networks: 236 waterfalls in the Waipaoa River, North Island, New Zealand. *Geomorphology*, *82*(1-2), 16–38. doi: 10.1016/j.geomorph.2005.08.023

Cyr, A. J., Granger, D. E., Olivetti, V., & Molin, P. (2010, June). Quantifying rock uplift rates using channel steepness and cosmogenic nuclide–determined erosion rates: Examples from northern and southern Italy. *Lithosphere*, *2*(3), 188–198. doi: 10.1130/L96.1

Davis, W. M. (1899). The Geographical Cycle. *The Geographical Journal*, *14*(5), 481. doi: 10.2307/1774538

de Lapparent, A. (1896). *Leçons de géographie physique.* Paris: Masson et c', éditeurs.

DeLong, S. B., Hilley, G. E., Prentice, C. S., Crosby, C. J., & Yokelson, I. N. (2017). Geomorphology , denudation rates , and stream channel profiles reveal patterns of mountain building adjacent to the San Andreas fault in northern California , USA. *GSA Bulletin*, *129*(5), 732–749. doi: 10.1130/B31551.1

DiBiase, R. A., Whipple, K. X., Heimsath, A. M., & Ouimet, W. B. (2010, January). Landscape form and millennial erosion rates in the San Gabriel Mountains, CA. *Earth and Planetary Science Letters*, *289*(1-2), 134–144. doi: 10.1016/j.epsl.2009.10.036

Flint, J. J. (1974). Stream gradient as a function of order, magnitude, and discharge. *Water Resources Research*, *10*(5), 969–973. doi: 10.1029/WR010i005p00969

Forte, A. M., & Whipple, K. X. (2018). Criteria and tools for determining drainage divide stability. *Earth and Planetary Science Letters*, *493*, 102–117.

Gailleton, B., Mudd, S. M., Clubb, F. J., Peifer, D., & Hurst, M. D. (2019). A segmentation approach for the reproducible extraction and quantification of knickpoints from river long profiles. *Earth Surface Dynamics*, *7*(1), 211–230. doi: 10.5194/esurf-7-211-2019

Gasparini, N. M., Tucker, G. E., & Bras, R. L. (2004). Network-scale dynamics of grain-size sorting: implications for downstream fining, stream-profile concavity, and drainage basin morphology. *Earth Surface Processes and Landforms*, *29*(4), 401–421. doi: 10.1002/esp.1031

Gilbert, G. K. (1880). *Report on the geology of the henry mountains.* US Government Printing Office.

Goren, L., Fox, M., & Willett, S. D. (2014, August). Tectonics from fluvial topography using formal linear inversion: Theory and applications to the Inyo Mountains, California. *Journal of Geophysical Research: Earth Surface*, *119*(8), 1651–1681. doi: 10.1002/2014JF003079

Gupta, S. (1997, January). Himalayan drainage patterns and the origin of fluvial megafans in the Ganges foreland basin. *Geology*, *25*(1), 11–14. (Publisher: GeoScienceWorld) doi: 10.1130/0091-7613(1997)025⟨0011:HDPATO⟩2.3.CO;2

Hack, J. (1957). *Studies of longitudinal profiles in Virginia and Maryland* (U.S. Geological Survey Professional Paper No. 294-B). Washington, D.C.: United States Government Printing Office.

Harel, M. A., Mudd, S. M., & Attal, M. (2016, September). Global analysis of the stream power law parameters based on worldwide 10be denudation rates. *Geomorphology*, *268*, 184–196. doi: 10.1016/j.geomorph.2016.05.035

Hergarten, S., Robl, J., & Stüwe, K. (2016, January). Tectonic geomorphology at small catchment sizes – extensions of the stream-power approach and the χ method. *Earth Surface Dynamics*, *4*(1), 1–9. doi: 10.5194/esurf-4-1-2016

Kirby, E., & Whipple, K. (2001). Quantifying differential rock-uplift rates via stream prole analysis. , 4.

Kirby, E., & Whipple, K. X. (2012, November). Expression of active tectonics in erosional landscapes. *Journal of Structural Geology*, *44*, 54–75. doi: 10.1016/j.jsg.2012.07.009

Knopf, E. B. (1924, sep). Correlation of residual erosion surfaces in the eastern appalachian highlands. *Bulletin of the Geological Society of America*, *35*(3), 633–668. doi: 10.1130/GSAB-35-633

Lague, D. (2014, January). The stream power river incision model: Evidence, theory and beyond. *Earth Surface Processes and Landforms*, *39*(1), 38–61. doi: 10.1002/esp.3462

Lal, D. (1991, June). Cosmic ray labeling of erosion surfaces: in situ nuclide production rates and erosion models. *Earth and Planetary Science Letters*, *104*(2), 424–439. doi: 10.1016/0012-821X(91)90220-C

Lavé, J., & Avouac, J. P. (2001). Fluvial incision and tectonic uplift across the

Himalayas of central Nepal. *Journal of Geophysical Research: Solid Earth*, *106*(B11), 26561–26591.

Leever, K. A., Matenco, L., Garcia-Castellanos, D., & Cloetingh, S. A. (2011, apr). The evolution of the Danube gateway between Central and Eastern Paratethys (SE Europe): Insight from numerical modelling of the causes and effects of connectivity between basins and its expression in the sedimentary record. *Tectonophysics*, *502*(1-2), 175–195. doi: 10.1016/j.tecto.2010.01.003

Leever, K. A., Matenco, L., Rabagia, T., Cloetingh, S., Krijgsman, W., & Stoica, M. (2010, feb). Messinian sea level fall in the Dacic Basin (Eastern Paratethys): Palaeogeographical implications from seismic sequence stratigraphy. *Terra Nova*, *22*(1), 12–17. doi: 10.1111/j.1365-3121.2009.00910.x

Lehner, B., Verdin, K., & Jarvis, A. (2008, mar). New global hydrography derived from spaceborne elevation data. *Eos*, *89*(10), 93–94. doi: 10.1029/2008EO100001

Lindvall, S. C., & Rubin, C. M. (2008). *Slip Rate Studies along the Sierra Madre–Cucamonga Fault System Using Geomorphic and Cosmogenic Surface Exposure Age Constraints: Collaborative Research with Central Washington University and William Lettis & Associates, Inc.* (Tech. Rep. No. US Geological Survey final report 03HQGR0084).

Mandal, S. K., Lupker, M., Burg, J.-P., Valla, P. G., Haghipour, N., & Christl, M. (2015, September). Spatial variability of 10be-derived erosion rates across the southern Peninsular Indian escarpment: A key to landscape evolution across passive margins. *Earth and Planetary Science Letters*, *425*, 154–167. doi: 10.1016/j.epsl.2015.05.050

Matenco, L., Andriessen, P., et al. (2013). Quantifying the mass transfer from mountain ranges to deposition in sedimentary basins: Source to sink studies in the danube basin–black sea system. *Global and planetary change*, *103*, 1–18.

Maţenco, L. (2017). Tectonics and exhumation of Romanian carpathians: Inferences from kinematic and thermochronological studies. In M. Radoane & A. Vespremeanu-Stroe (Eds.), *Springer geography* (pp. 15–56). Cham: Springer International Publishing. doi: 10.1007/978-3-319-32589-7_2

Mitchell, N. A., & Yanites, B. J. (2019). Spatially Variable Increase in Rock Uplift in the Northern U.S. Cordillera Recorded in the Distribution of River Knickpoints and Incision Depths. *Journal of Geophysical Research: Earth Surface*, *124*(5), 1238–1260. doi: 10.1029/2018JF004880

Morisawa, M. E. (1962, September). Quantitative Geomorphology of Some Watersheds in the Appalachian Plateau. *GSA Bulletin*, *73*(9), 1025–1046. doi: 10.1130/0016-7606(1962)73[1025:QGOSWI]2.0.CO;2

Mudd, S. M., Attal, M., Milodowski, D. T., Grieve, S. W., & Valters, D. A. (2014, feb). A statistical framework to quantify spatial variation in channel gradients using the integral method of channel profile analysis. *Journal of Geophysical Research: Earth Surface*, *119*(2), 138–152. doi: 10.1002/2013JF002981

Mudd, S. M., Clubb, F. J., Gailleton, B., & Hurst, M. D. (2018, jun). How concave are river channels? *Earth Surface Dynamics*, *6*(2), 505–523. doi: 10.5194/esurf-6-505-2018

Niemann, J. D., Gasparini, N. M., Tucker, G. E., & Bras, R. L. (2001, November). A quantitative evaluation of Playfair's law and its use in testing long-term stream erosion models. *Earth Surface Processes and Landforms*, *26*(12), 1317–1332. doi: 10.1002/esp.272

Ouimet, W. B., Whipple, K. X., & Granger, D. E. (2009, July). Beyond threshold hillslopes: Channel adjustment to base-level fall in tectonically active mountain ranges. *Geology*, *37*(7), 579–582. doi: 10.1130/G30013A.1

Perron, J. T., & Royden, L. H., Royden. (2013). An integral approach to bedrock river profile analysis. *Earth Surface Processes and Landforms*, *38*(6), 570–576. doi: 10.1002/esp.3302

Pike, A. S., Scatena, F. N., & Wohl, E. E. (2010). Lithological and fluvial controls on the geomorphology of tropical montane stream channels in puerto rico. *Earth Surface Processes and Landforms*, *35*(12), 1402-1417. Retrieved from `https://onlinelibrary.wiley.com/doi/abs/10.1002/esp.1978` doi: https://doi.org/10.1002/esp.1978

Playfair, J. (1802). *Illustrations of the Huttonian theory of the earth.* Edinburgh: Neill and Co. Printers.

Prince, P. S., & Spotila, J. A. (2013). Evidence of transient topographic disequilibrium in a landward passive margin river system: knickpoints and paleolandscapes of the New River basin, southern Appalachians. *Earth Surface Processes and Landforms*, *38*(14), 1685–1699. doi: 10.1002/esp.3406

Ringenbach, J. C., Pinet, N., Delteil, J., & Stephan, J. F. (1992). Analyse des structures engendrees en regime decrochant par le seisme de Nueva Ecija du 16 juillet 1990, Luzon, Philippines. *Bulletin - Societe Geologique de France*, *163*(2), 109–123.

Royden, L. H., K., C. M., & Whipple, K. X. (2000). Evolution of river elevation profiles by bedrock incision; analytical solutions for transient river profiles related to changing uplift and precipitation rates. In *Eos, transactions, american geophysical union* (Vol. 81, pp. 1–2). Fall Meeting Supplement.

Royden, L. H., & Perron, J. (2013). Solutions of the stream power equation and application to the evolution of river longitudinal profiles. *Journal of Geophysical Research: Earth Surface*, *118*(2), 497–518. doi: 10.1002/jgrf.20031

Safran, E. B., Bierman, P. R., Aalto, R., Dunne, T., Whipple, K. X., & Caffee, M. (2005). Erosion rates driven by channel network incision in the Bolivian Andes. *Earth Surface Processes and Landforms*, *30*(8), 1007–1024. doi: 10.1002/esp.1259

Scherler, D., Bookhagen, B., & Strecker, M. R. (2014, February). Tectonic control on 10be-derived erosion rates in the Garhwal Himalaya, India. *Journal of Geophysical Research: Earth Surface*, *119*(2), 83–105. doi: 10.1002/2013JF002955

Schoenbohm, L. M., Whipple, K. X., Burchfiel, B. C., & Chen, L. (2004, July). Geomorphic constraints on surface uplift, exhumation, and plateau growth in the Red River region, Yunnan Province, China. *GSA Bulletin*, *116*(7-8), 895–909. doi: 10.1130/B25364.1

Seagren, E., & Schoenbohm, L. (2019). Base level and lithologic control of drainage reorganization in the sierra de las planchadas, nw argentina. *Journal of Geophysical Research: Earth Surface*, *124*, 1516–1539. doi: 10.1029/2018JF004885

Seeber, L., & Gornitz, V. (1983, March). River profiles along the Himalayan arc as indicators of active tectonics. *Tectonophysics*, *92*(4), 335–367.

Shelef, E., Haviv, I., & Goren, L. (2018, March). A potential link between waterfall recession rate and bedrock channel concavity. *Journal of Geophysical Research: Earth Surface*, *0*(0). doi: 10.1002/2016JF004138

Snyder, N. P. (2000). Landscape response to tectonic forcing: Digital elevation model analysis of stream profiles in the Mendocino triple junction region, northern California. *Geological Society of America Bulletin*, 14.

Stock, J., & Dietrich, W. E. (2003). Valley incision by debris flows: Evidence of a topographic signature. *Water Resources Research*, *39*(4). doi: 10.1029/2001WR001057

Struth, L., Garcia-Castellanos, D., Viaplana-Muzas, M., & Vergés, J. (2019, February). Drainage network dynamics and knickpoint evolution in the Ebro and Duero basins: From endorheism to exorheism. *Geomorphology*, *327*, 554–571.

ter Borgh, M. M. (2013). *Connections between sedimentary basins during continental collision* (Unpublished doctoral dissertation).

Tucker, G. E., & Whipple, K. X. (2002). Topographic outcomes predicted by stream

erosion models: Sensitivity analysis and intermodel comparison. *Journal of Geophysical Research: Solid Earth*, *107*(B9), ETG 1–1–ETG 1–16. doi: 10.1029/2001JB000162

Whipple, K. X. (2004). Bedrock Rivers and the Geomorphology of Active Orogens. *Annual Review of Earth and Planetary Sciences*, *32*(1), 151–185. doi: 10.1146/annurev.earth.32.101802.120356

Whipple, K. X., DiBiase, R. A., & Crosby, B. T. (2013, mar). Bedrock Rivers. In *Treatise on geomorphology* (Vol. 9, pp. 550–573). Elsevier Inc. doi: 10.1016/B978-0-12-374739-6.00254-2

Whipple, K. X., DiBiase, R. A., Ouimet, W. B., & Forte, A. M. (2017, January). Preservation or piracy: Diagnosing low-relief, high-elevation surface formation mechanisms. *Geology*, *45*(1), 91–94. doi: 10.1130/G38490.1

Whipple, K. X., & Tucker, G. E. (1999). Dynamics of the stream-power river incision model: Implications for height limits of mountain ranges, landscape response timescales, and research needs. *Journal of Geophysical Research: Solid Earth*, *104*(B8), 17661–17674. doi: 10.1029/1999JB900120

Whittaker, A. C. (2012). How do landscapes record tectonics and climate? *Lithosphere*, *4*(2), 160–164. doi: 10.1130/RF.L003.1

Whittaker, A. C., & Boulton, S. J. (2012). Tectonic and climatic controls on knickpoint retreat rates and landscape response times. *Journal of Geophysical Research: Earth Surface*, *117*(F2).

Wickert, A. D., & Schildgen, T. F. (2019, January). Long-profile evolution of transport-limited gravel-bed rivers. *Earth Surface Dynamics*, *7*(1), 17–43. doi: https://doi.org/10.5194/esurf-7-17-2019

Willett, S. D., McCoy, S. W., Perron, J. T., Goren, L., & Chen, C.-Y. (2014, March). Dynamic Reorganization of River Basins. *Science*, *343*(6175), 1248765–1248765. doi: 10.1126/science.1248765

Wobus, C. W., Crosby, B. T., & Whipple, K. X. (2006, June). Hanging valleys in fluvial systems: Controls on occurrence and implications for landscape evolution. *Journal of Geophysical Research: Earth Surface*, *111*(F2), F02017. doi: 10.1029/2005JF000406

Yin, A. (2006, May). Cenozoic tectonic evolution of the Himalayan orogen as constrained by along-strike variation of structural geometry, exhumation history, and foreland sedimentation. *Earth-Science Reviews*, *76*(1), 1–131.

Zaprowski, B. J., Pazzaglia, F. J., & Evenson, E. B. (2005). Climatic influences on profile concavity and river incision. *Journal of Geophysical Research: Earth Surface*, *110*, F03004. doi: 10.1029/2004JF000138

Zhang, Y., Hassan, M. A., King, L., Fu, X., Istanbulluoglu, E., & Wang, G. (2020). Morphometrics of China's Loess Plateau: The spatial legacy of tectonics, climate, and loess deposition history. *Geomorphology*, *354*, 107043. doi: 10.1016/j.geomorph.2020.107043